Kinetics of $L1_0$-type and $L1_2$-type orderings in alloys at early stages of phase transformations

2001 J. Phys.: Condens. Matter 13 6031

(http://iopscience.iop.org/0953-8984/13/26/318)

INSTITUTE OF PHYSICS PUBLISHING JOURNAL OF PHYSICS: CONDENSED MATTER

J. Phys.: Condens. Matter **13** (2001) 6031–6058 www.iop.org/Journals/cm PII: S0953-8984(01)15117-9

Kinetics of $L1_0$-type and $L1_2$-type orderings in alloys at early stages of phase transformations

I R Pankratov and V G Vaks

Russian Research Centre 'Kurchatov Institute', Moscow 123182, Russia

Received 3 July 2000, in final form 2 March 2001

Abstract

We study the kinetics of the $L1_0$ ordering in face-centred alloys at early stages of phase transformations, when the tetragonal distortion of the $L1_0$ phase is still insignificant as regards the microstructural evolution, and compare it with the kinetics of the $L1_2$ ordering. We use the earlier-described kinetic cluster-field method to simulate $A1 \rightarrow L1_0$ and $A1 \rightarrow L1_2$ transformations after a quench of an alloy from the disordered A1 phase to the single-phase $L1_0$ or $L1_2$ state for a number of alloy models with both short-range and extended-range interactions. The simulations reveal a number of peculiar features in both transient microstructures and transformation kinetics—in particular, a sharp dependence of the microstructural evolution and the structure of antiphase boundaries under the $L1_0$ ordering on the composition of the alloy; the importance for both the $L1_0$ and $L1_2$ ordering of a peculiar mechanism of domain growth via the fusion of different in-phase domains; the presence in transient microstructures under the $L1_0$ ordering of some specific long-living configurations, quadruple junctions of four different antiphase domains, as well as of peculiar kinetic processes of 'splitting' of certain antiphase boundaries into two others; and other features.

1. Introduction

Studies of microstructural evolution in ordering phase transformations of alloys attract interest from both fundamental and applied points of view. From the fundamental side, the creation and evolution of ordered domains provide classical examples of the self-organization phenomena being discussed in many areas of physics and chemistry. From the applied side, the microstructural features of an ordered alloy, such as the distribution and morphology of antiphase boundaries (APBs) separating the antiphase-ordered domains (APDs), can significantly affect the macroscopic properties, for example, strength, plasticity, coercivity of ferromagnets, and others. There are many theoretical studies of microstructural evolution under alloy ordering, e.g. [1–5]. However, most of these works [1–4] treat only the simplest B2 ordering with just two types of APD and one type of APB between them. Meanwhile, ordered structures in real alloys are usually much more complex and include many types of APD and APB. For example, under the $L1_2$ ordering (Cu_3Au type) on the FCC lattice there are four

0953-8984/01/266031+28$30.00

types of APD, while under the $L1_0$ ordering (CuAu I type) there are six types of APD and two different types of APB separating the APDs with the same or with perpendicular tetragonal axes. In addition to that, each APB under the $L1_2$ or $L1_0$ ordering, depending on its structure and orientation, can be either 'conservative' or 'non-conservative', and the morphological and kinetic properties for these two types of APB are quite different [6, 7]. The 'multivariant' character of ordering can result in a number of specific kinetic features that are absent for the simplest B2 ordering [7, 8]. In our previous paper [7] we discussed these features for the $L1_2$-type orderings. In the present work we extend this study to the $L1_0$ ordering and compare it with the $L1_2$ ordering.

Features of microstructural evolution after a quench of an alloy from the disordered FCC phase (A1 phase) to the single-phase $L1_0$ state have been experimentally studied by many authors; see e.g. [9–12]. However, there seem to be few theoretical treatments of these problems. To avoid discussing the problems of nucleation, in this work we consider transformation temperatures T lower than the ordering spinodal temperature T_s. Then the microstructural evolution under the A1 $\rightarrow$ $L1_0$ transition includes the following stages [9–12]:

(A) The initial stage of the formation of finest $L1_0$-ordered domains when their tetragonal distortion still has little effect on the microstructural evolution and all six types of APD are present in microstructures in the same proportion. For real alloys it usually corresponds to a characteristic APD size l_d of the order of or less than 5–10 lattice parameters a (i.e. $l_d \lesssim$ 2–5 nm) and to the so-called 'mottled' contrast in the transmission electron microscopy (TEM) images [10, 11].

(B) The next, intermediate stage which corresponds to the so-called 'tweed' contrast in TEM images and to typical APD sizes $l_d \sim$ (10–30)a. The tetragonal deformation of the $L1_0$-ordered APDs here leads to a noticeable predominance of the (110)-oriented APBs in the microstructures, but all six types of APD (i.e. all three orientations of the tetragonal axis c) are still present in similar proportions [9, 12].

(C) The final, 'polytwinned' stage when the tetragonal distortion of the $L1_0$-ordered APDs becomes the main factor determining the microstructural evolution and leads to the formation of the (110)-type-oriented bands with a width $d \gtrsim 50a$ and a length $l \gg d$. Each band includes only two types of APD with the same c-axis, and these axes in the adjacent bands are 'twin' related, i.e. have the alternate (100) and (010) orientations for the given set of the (110)-oriented bands [9, 12].

Because of considerations of space, in this paper we discuss only the initial stage (A), when the tetragonal distortion of the $L1_0$-ordered APDs and the deformational interactions related to this distortion are still insignificant for the evolution and will be neglected. These deformational interactions will be considered in a separate paper where we also discuss the 'tweed' and 'twin' stages of evolution and show that the main microstructural features of the initial stage (A) discussed in the present work are also characteristic for the next, 'tweed' stage (B).

To study the kinetics of the A1 $\rightarrow$ $L1_0$ transition we employ the master equation approach to configurational kinetics of alloys described in references [13] and [14]. Evolution of an alloy in this approach is described by a certain set of exact equations for local concentrations and their correlators. To solve these equations one can use various approximate methods analogous to those employed in equilibrium statistical physics, for example, the kinetic mean-field approximation (KMFA) [2,3,8] which is a generalization of the mean-field approximation (MFA) of equilibrium statistical physics to the case of inhomogeneous and non-stationary distributions. However, to describe ordering phase transitions in the FCC alloys, such as the $L1_0$ and $L1_2$ orderings, the simple MFA is insufficient and more exact, cluster methods should be used, such as the cluster variation method (CVM) [15, 16] or its simplified version,

the cluster-field method (CFM) [17]. In reference [7] (to be referred to as I) we described a kinetic generalization of CFM suitable for treatments of the $L1_2$ and $L1_0$ orderings, the kinetic tetrahedron cluster-field method (KTCFM), and applied it in studies of some problems of kinetics of the $L1_2$-type orderings. In the present work we employ the KTCFM to investigate kinetics of both the $L1_0$ and $L1_2$ orderings.

We use the KTCFM to simulate A1 $\rightarrow$ $L1_0$ and A1 $\rightarrow$ $L1_2$ transitions for a number of alloy models with both short-range and extended-range chemical interactions. It enables us to elucidate, in particular, the dependence of the microstructural evolution on the interaction type which turns out to be very sharp for both the $L1_0$ and $L1_2$ ordering. Our simulation also reveals a number of peculiar microstructural features of the A1 $\rightarrow$ $L1_0$ transformation. Some of them are analogous to those found in I for the $L1_2$ ordering, but some are absent for that simpler ordering. To more fully compare the microstructural evolution under the $L1_0$ and $L1_2$ orderings, in this work we also consider the two problems of the $L1_2$ ordering which have been just briefly mentioned in I, namely, the concentration dependence of the evolution and a peculiar mechanism of the APD growth via the fusion of in-phase domains. For the $L1_0$ ordering both the concentration dependence of the evolution and the fusion-of-domain mechanism of the evolution turn out to be still more pronounced than for the $L1_2$ ordering, and a detailed comparison helps us to understand the origin of the difference.

The paper is organized as follows. In section 2 we briefly describe the methods of simulation which are the same as in I. In section 3 we discuss the concentration dependence of the microstructural evolution and the fusion-of-domain processes for the A1 $\rightarrow$ $L1_2$ transformation. In section 4 we investigate the kinetics of the A1 $\rightarrow$ $L1_0$ transition for the short-range interaction systems, and in section 5, that for the systems with a larger interaction range. Our main conclusions are summarized in section 6.

2. Models and methods of simulation

To simulate both the A1 $\rightarrow$ $L1_0$ and A1 $\rightarrow$ $L1_2$ transformation we use the KTCFM and the same models and methods as were used in I. For the reader's convenience, below we briefly describe the main relations used.

We consider a binary substitutional alloy A–B. Various distributions of atoms over lattice sites i are described by the sets of occupation numbers $\{n_i\}$ where the operator $n_i = n_{Ai}$ is unity when the site i is occupied by atom A and zero otherwise. The interaction Hamiltonian H has the form

$$H = \sum_{i>j} v_{ij} n_i n_j + \sum_{i>j>k} v_{ijk} n_i n_j n_k + \cdots \tag{1}$$

where $v_{i\ldots j}$ are effective interactions, and for simplicity we consider the pair interaction model when equation (1) includes only the first term.

Evolution of atomic distributions in the KTCFM is described by the set of equations (I.10) for mean occupations $c_i = \langle n_i \rangle$ averaged over the time- and space-dependent distribution function:

$$\mathrm{d}c_i/\mathrm{d}t = 2 \sum_j M_{ij} \sinh[\beta(\lambda_j - \lambda_i)/2]. \tag{2}$$

Here $\beta = 1/T$ is the reciprocal temperature; λ_i is the local chemical potential; and M_{ij} is the generalized mobility proportional to the configurationally independent factor γ_{nn} in the probability of an inter-site atomic exchange $A_i \leftrightarrow B_j$ between neighbouring sites i and j per unit time. The microscopical expressions for $\lambda_i = \lambda_i\{c_j\}$ employed in our simulations are

given by equations (I.13)–(I.16), and for $M_{ij} = M_{ij}\{c_k\}$ we use the expression (I.12) with the asymmetrical potential u_i taken as zero for simplicity.

To simulate both the A1 $\rightarrow$ $L1_0$ and A1 $\rightarrow$ $L1_2$ transitions we employ the five alloy models used in I:

(1) The second-neighbour interaction model with $v_2/v_1 = \epsilon = -0.125$.
(2) The same model with $\epsilon = -0.25$.
(3) The same model with $\epsilon = -0.5$.
(4) The fourth-neighbour interaction model with v_n estimated by Chassagne *et al* [18] from their experimental data for disordered Ni–Al alloys (in units of the Boltzmann constant k_B): $v_1 = 1680$ K, $v_2 = -210$ K, $v_3 = 35$ K, and $v_4 = -207$ K.
(5) The fourth-neighbour interaction model with $v_2/v_1 = -0.5$, $v_3/v_1 = 0.25$, and $v_4/v_1 = -0.125$.

The effective interaction range R_{int} for these models monotonically increases with the model number. Therefore, a comparison of the simulation results for these models can provide information about the influence of R_{int} on the microstructural evolution. Let us also note that the reduced temperature $T_c' = T_c/v_1$ of the phase transition A1 $\rightarrow$ $L1_0$ at the stoichiometric composition $c = 0.5$ for models 1, 2, 3, 4, and 5 is 0.61, 0.84, 1.29, 1.16, and 2.28, respectively.

As was discussed in [7,8], the distribution of mean occupations c_i under alloy ordering can be described in terms of both long-ranged and local order parameters. For the homogeneous $L1_2$ or $L1_0$ ordering the distribution of $c_i = c(\boldsymbol{R}_i)$ (where $\boldsymbol{R}_i$ is the FCC lattice vector) can be written in terms of three long-ranged order parameters η_α; see e.g. [**?**]:

$$c_i = c + \eta_1 \exp(\mathrm{i}\boldsymbol{k}_1 \cdot \boldsymbol{R}_i) + \eta_2 \exp(\mathrm{i}\boldsymbol{k}_2 \cdot \boldsymbol{R}_i) + \eta_3 \exp(\mathrm{i}\boldsymbol{k}_3 \cdot \boldsymbol{R}_i) \tag{3}$$

where $\boldsymbol{k}_\alpha$ is the superstructure vector corresponding to η_α:

$$\boldsymbol{k}_1 = [100]2\pi/a \qquad \boldsymbol{k}_2 = [010]2\pi/a \qquad \boldsymbol{k}_3 = [001]2\pi/a. \tag{4}$$

For the cubic $L1_2$ structure $|\eta_1| = |\eta_2| = |\eta_3|$, $\eta_1\eta_2\eta_3 > 0$, and four types of ordered domain are possible. In the $L1_0$-ordered structure with the tetragonal axis α, a single non-zero parameter η_α is present which is either positive or negative. Therefore, six types of ordered domain are possible with two types of APB. That separation of two APDs with the same tetragonal axis will be for brevity called the 'shift-type APB' or 'shift-APB', and that separation of the APDs with perpendicular tetragonal axes will be called the 'flip-type APB' or 'flip-APB'.

The transient partially ordered alloy states including APBs can be conveniently described in terms of local squared order parameters $\eta_{\alpha i}^2$ and local concentrations $\bar{c}_i$ which correspond to a spatial averaging over a nearest neighbourhood of each site i [7]:

$$\eta_{\alpha i}^2 = \frac{1}{16}\left[c_i + \frac{1}{4}\sum_{j=\mathrm{nn}(i)} c_j \exp(\mathrm{i}\boldsymbol{k}_\alpha \cdot \boldsymbol{R}_{ji})\right]^2 \qquad \bar{c}_i = \frac{1}{4}\left(c_i + \frac{1}{4}\sum_{j=\mathrm{nn}(i)} c_j\right). \tag{5}$$

Here $\mathrm{nn}(i)$ means the summation over nearest neighbours of site i; $\boldsymbol{R}_{ji}$ is $\boldsymbol{R}_j - \boldsymbol{R}_i$; and the coefficients on the right-hand side are chosen such that in the homogeneous case (3) we would have $\eta_{\alpha i}^2 = \eta_\alpha^2$, $\bar{c}_i = c$.

As was discussed in I, the description of alloy states in terms of the distribution of mean site occupations c_i (to be called the 'c-representation') is convenient for describing the atomic-scale microstructures, while the evolution of extended ordered domains is more conveniently described in terms of the local order parameter distributions. These distributions are similar to those observed in TEM images where the reflection intensity is proportional to the squared value of the relevant order parameter [19]. Thus the simulation results below are usually presented

as the distributions of quantities $\eta_i^2 = \eta_{1i}^2 + \eta_{2i}^2 + \eta_{3i}^2$ (to be called the 'η^2-representation') which can be directly compared with experimental TEM images.

Our simulations were performed in FCC simulation boxes of sizes $V_b = L^2 \times H$ (where L and H are given in units of the lattice constant a) with periodic boundary conditions. We used both quasi-2D simulations with $H = 1$ and 3D simulation with $H = L$. Employing 2D models is a usual method for extending the maximum size of microstructures examined [1–4, 7, 8] but below (as well as in I) the conclusions derived from 2D simulations are also complemented with 3D simulation. For the given coordinate $z = na$ (with $n = 0$ for 2D simulation) each of figures 1–5, 7–11, and 13–17 below shows all FCC lattice sites lying in two adjacent planes, $z = na$ and $z = (n+1/2)a$. The point (x, y) with $(x/a, y/a)$ equal to (l, m), $(l+1/2, m)$, $(l+1/2, m+1/2)$, or $(l, m + 1/2)$ in these figures corresponds to the lattice site with $(x/a, y/a, z/a)$ equal to (l, m, n), $(l + 1/2, m, n + 1/2)$, $(l + 1/2, m + 1/2, n)$, or $(l, m + 1/2, n + 1/2)$, respectively. Therefore, at $V_b = L^2 \times H$ the figure shows $4L^2$ lattice sites.

The simulation methods were the same as in references [2, 3, 7, 8]. In the simulations of the A1 $\rightarrow$ $L1_0$ transition the transformation temperature T for each model was taken equal or close to that used in I for the A1 $\rightarrow$ $L1_2$ transition in the same model. The ratio of this T to the $L1_0$ ordering critical temperature T_c is approximately the same for all models: $T/T_c \simeq 0.6$, thus the influences of the temperature on the evolution for the different models are similar. In the simulations of both the A1 $\rightarrow$ $L1_0$ and A1 $\rightarrow$ $L1_2$ transformations the initial as-quenched distribution $c_i(0)$ was characterized by its mean value c and small random fluctuations δc_i; usually we used $\delta c_i = \pm 0.01$.

3. Concentration dependence of microstructural evolution and the 'fusion-of-domain' mechanism of domain growth under the $L1_2$ ordering

Kinetic features of the A1 $\rightarrow$ $L1_2$ transformation have been discussed in I mainly for the stoichiometric composition $c = 0.25$. It was shown that the microstructural evolution sharply depends on the interaction type, particularly on the interaction range R_{int}. For the short-range-interaction systems, such as our models 1, 2, and 3, transient microstructures include mainly the conservative APBs (c-APBs) which lie in the main crystal planes with (100)-type orientation and correspond to a certain relation between this orientation and the type of two adjacent ordered domains: the translation vector relating these APDs lies within the c-APB plane [6, 19]. In addition to that, the conservative APBs are usually notably thinner than other, non-conservative APBs. All these features of c-APBs are illustrated by figure 1 which complements analogous figures shown in I with the indication of the APD type. The label A, B, C, or D in this figure indicates an APD in which the minority atoms fill the sublattice with the basis vector (0, 0, 0), (0, 0.5, 0.5), (0.5, 0.5, 0), or (0.5, 0, 0.5), respectively, in the FCC lattice elementary cube. In accordance with the above-mentioned relation between the type of domains adjacent to a c-APB, for the edge-on APBs shown in figure 1 the vertical c-APBs are present only between domains A and B or C and D; the horizontal c-APBs are present only between domains A and C or B and D; while the APBs between domains A and D or B and C are always non-conservative. For the nearest-neighbour-interaction model with $v_{n>1} = 0$ the c-APBs have zero excess energy, unlike non-conservative APBs [6]. Therefore, for the second-neighbour-interaction models with small $\epsilon = v_2/v_1$ this excess energy is also small which explains the predominance of c-APBs in the microstructures for such systems.

With an increase of the interaction range R_{int} the energetic preference of conservative APBs with respect to non-conservative ones diminishes, which results in a decrease of the relative number of conservative APBs in the microstructures. In the simulations for model 4 at $c = 0.25$ the conservative APBs are few but still observable, while for model 5 with a larger R_{int}

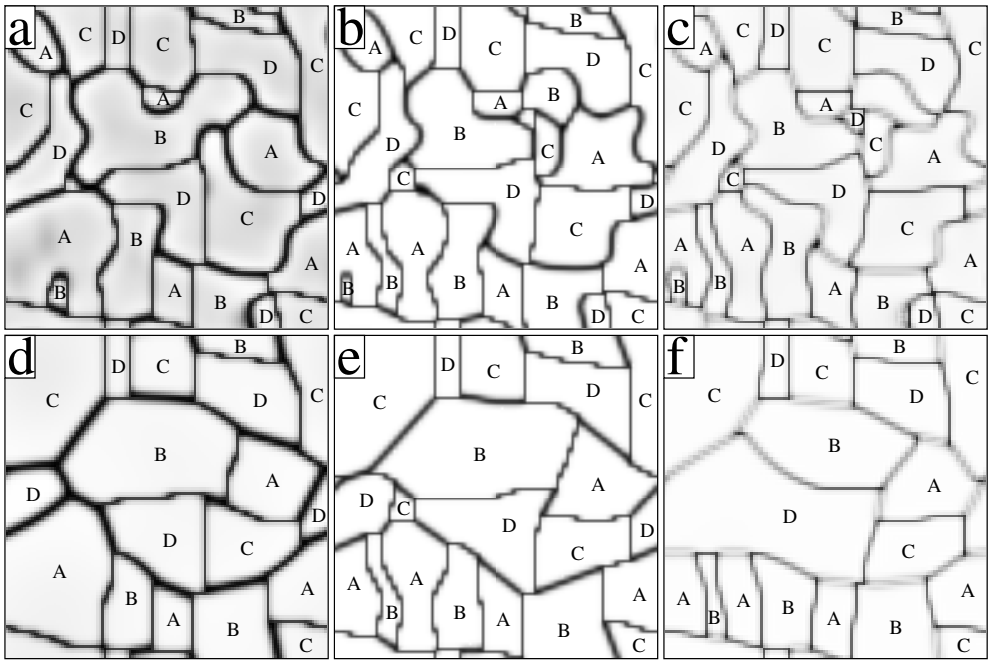

Figure 1. Temporal evolution of the second-neighbour-interaction model 2 with $\varepsilon = v_2/v_1 = -0.25$ under the phase transformation A1 $\rightarrow$ L1$_2$ shown in the η^2-representation for the simulation box size $V_b = 64^2 \times 1$ at $T' = T/v_1 = 0.5$ and the following values of the concentration c and the reduced time $t' = t\gamma_{nn}$: (a) $c = 0.22$, $t' = 10$; (b) $c = 0.25$, $t' = 10$; (c) $c = 0.32$, $t' = 10$; (d) $c = 0.22$, $t' = 200$; (e) $c = 0.25$, $t' = 200$; and (f) $c = 0.32$, $t' = 200$. The grey level linearly varies with $\eta_i^2 = \eta_{1i}^2 + \eta_{2i}^2 + \eta_{3i}^2$ between its minimum and maximum values from completely dark to completely bright. The label A, B, C, or D indicates the type of the ordered domain as described in the text.

such APBs are absent entirely. Below we show that similar variations of microstructures with the interaction range are also characteristic for the A1 $\rightarrow$ L1$_0$ transition. In accordance with these microstructural features, model 4 and model 5 will be considered below as representative of systems with an 'intermediate' and an 'extended' interaction range, respectively.

We also discussed in I an effect of non-stoichiometry on the evolution for model 2 and mentioned some 'fusion-of-domain' processes, but did not consider these points in detail. Below we show that both the concentration dependence of the evolution and the fusion-of-domain processes under the L1$_0$ ordering are still more pronounced than under the L1$_2$ ordering. To more fully compare the kinetics of these two orderings, in this section we consider these features of evolution for the A1 $\rightarrow$ L1$_2$ transition in more detail.

To complement the studies described in I we made KTCFM-based simulations of the A1 $\rightarrow$ L1$_2$ transition for models 4 and 5 at three concentrations: $c = c_- = 0.22$, $c = c_s = 0.25$, and $c = c_+ = 0.32$, using the same temperatures as in I, i.e. $T' = T/v_1 = 0.685$ ($T = 1150$ K) for model 4 and $T' = 1.34$ for model 5. The points (c_-, T) and (c_+, T) in the c–T plane for each of these models correspond to approximately the same distance $\delta c \simeq 0.02$ from the two-phase field, A1 + L1$_2$ and L1$_2$ + L1$_0$, respectively, just as for model 2 in I, and for both models 4 and 5 we used quasi-2D simulations with the simulation box volume $V_b = 128^2 \times 1$. The distribution of initial fluctuations δc_i for the given V_b was taken as the same for all models and concentrations treated in this work including simulations of the

A1 $\rightarrow$ $L1_0$ transition described below. At the same time, this distribution δc_i differs from that used in I for the same V_b which enables one to appreciate the effect of variations of this distribution on the microstructural evolution.

Some results of these simulations are presented in figures 2–5. As mentioned, the evolution shown in figures 2 or 5 corresponds to the same values of c and T as that shown in figures 8 or 9 in I (figures I.8 or I.9) but to different distribution of initial fluctuations δc_i. Comparison of figure 2 with I.8 or 5 with I.9 shows that the distribution of δc_i used in the present work results in a finer size of initial ordered domains and in a larger number of different APDs for the given evolution time (by about 1.5–2 times) compared to figures I.8 and I.9. It results, in particular, in a larger number of the fusion-of-domain processes discussed below in the scenarios shown in figures 2 and 5 compared to figures I.8 and I.9. However, all qualitative features of evolution discussed in I and illustrated by figures I.8 and I.9 are also clearly seen in figures 2 and 5. In particular, the microstructures for the intermediate-range-interaction model 4 in both figures I.8 and 2 include mainly non-conservative APBs. However, the (100)-oriented conservative APBs are present, too, and have a noticeable effect on microstructures, particularly at the later stages of evolution. For the extended-range-interaction model 5 the microstructures in both figures I.9 and 5 show neither conservative APBs nor anisotropy while the triple junctions of APBs form approximately equi-angle configurations characteristic of isotropic systems.

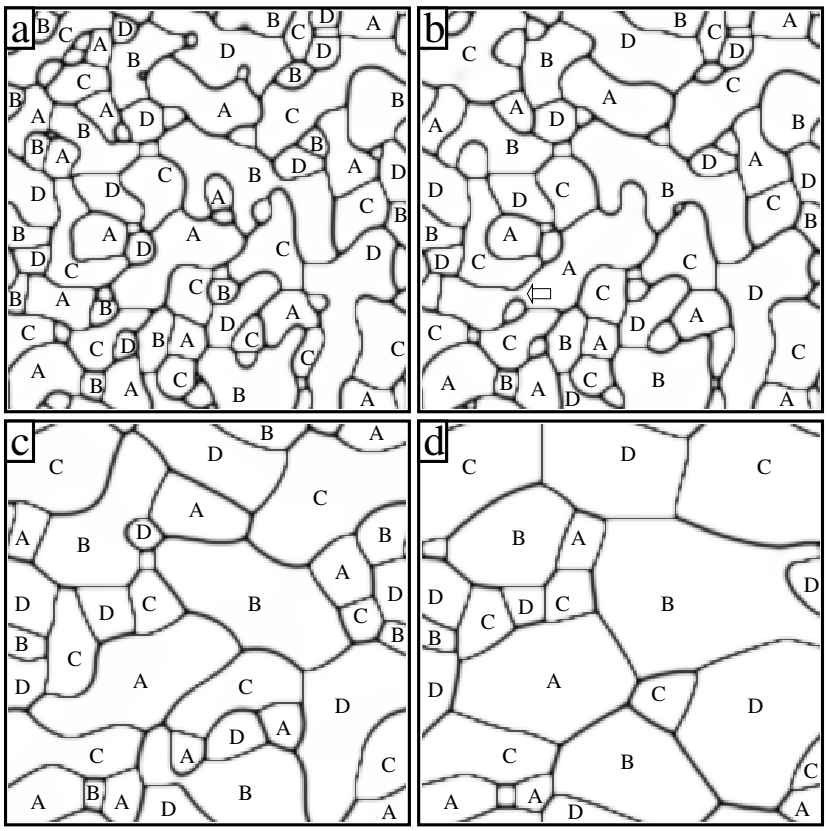

Figure 2. As figure 1, but for model 4 with $V_b = 128^2 \times 1$ at $T' = 0.685$ ($T = 1150$ K), $c = 0.25$, and the following values of $t' = t\gamma_{nn}$: (a) 5; (b) 10; (c) 50; and (d) 250. The thick arrows here and below indicate the fusion-of-domain processes discussed in the text.

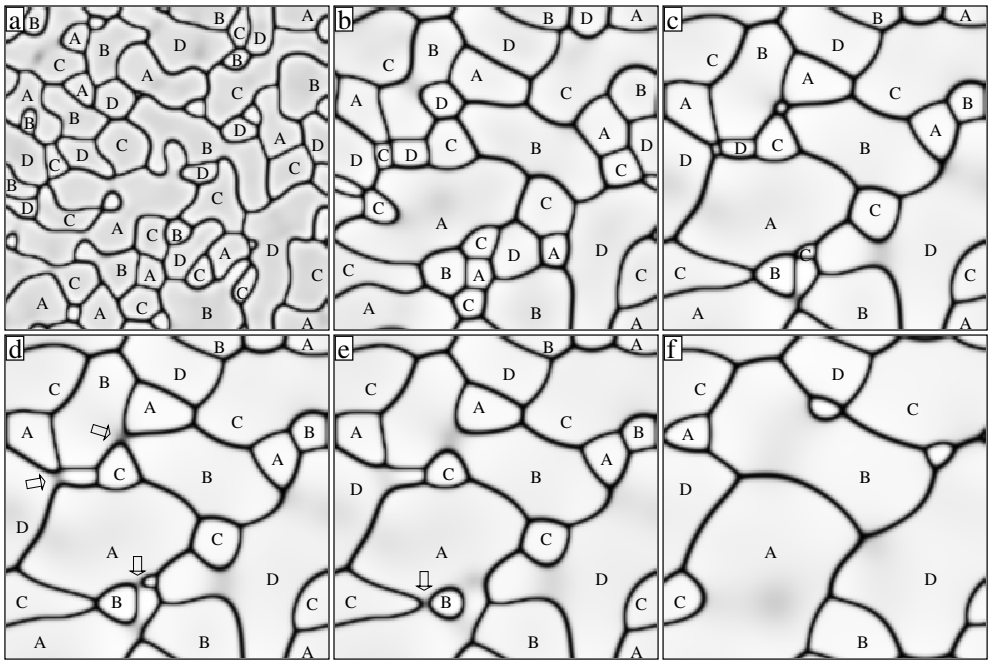

Figure 3. As figure 2, but at $c = 0.22$ and the following values of t': (a) 5; (b) 50; (c) 120; (d) 125; (e) 140; and (f) 250.

Therefore, variations of initial fluctuations δc_i do not seem to affect the qualitative features of evolution which are the main subject of the present study.

The concentration dependence of the evolution for model 4 is illustrated by figures 2, 3 and 4. The comparison with an analogous dependence for the short-range-interaction model 2 illustrated by figure 1 shows that for model 4 this dependence is much more pronounced. Microstructures for model 2 at the stoichiometric and non-stoichiometric concentrations c_s, c_-, and c_+ are similar, displaying, in particular, a strong tendency for the formation of (100)-oriented conservative APBs. The predominance of such APBs leads to a slowing down of evolution as the conservative APBs are virtually immobile [7]. In contrast, for model 4 the anisotropy in the distribution of APBs due to the presence of conservative APBs is noticeable only at the stoichiometric composition $c = c_s$ (figure 2), while at $c = c_+$ (figure 4) it is much weaker, and at $c = c_-$ (figure 3) it is absent entirely.

The reduction in the number of conservative APBs results in an increase of the evolution rate. This rate can be characterized, for example, by the total number N_d of different APDs in the microstructures (for the given evolution time) or by the mean APD size l_d which for the simulation box with $V_b = L^2 \times H$ can be defined as $l_d = aL/N_d^{1/2}$: the greater N_d and the smaller l_d, the lower the evolution rate. For the microstructures shown in frames 2(d), 3(f) and 4(d) (which correspond to the same reduced time $t' = 250$) the number N_d is 20, 10, and 11, and l_d/a is 30, 40, and 39, respectively, which illustrates the slowing down of evolution at the stoichiometric composition.

For the extended-range-interaction model 5 the influence of non-stoichiometry on the microstructural evolution is much weaker than for model 4 as conservative APBs here are absent even at the stoichiometric composition $c = 0.25$ (figure 5), so variations of composition have no qualitative effect on microstructures.

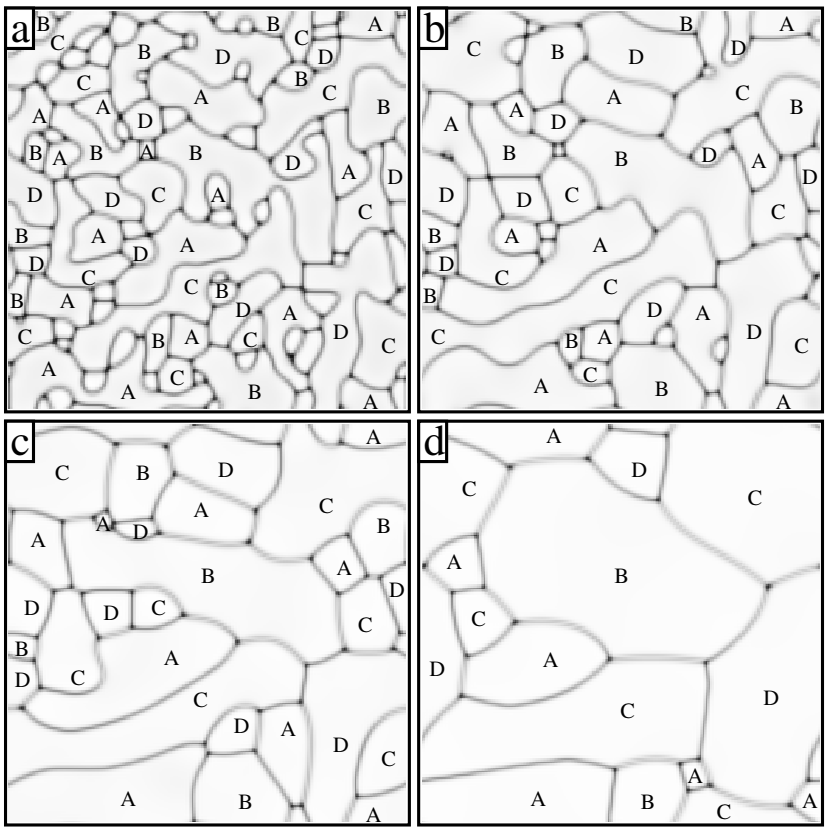

Figure 4. As figure 2, but at $c = 0.32$ and the following values of t': (a) 5; (b) 20; (c) 50; and (d) 250.

To more quantitatively characterize the influence of both the interaction range and the composition on evolution, in table 1 we present values of N_d, l_d and the proportion ν_c of conservative APBs for some microstructures observed in our simulations. The proportion ν_c is defined as the ratio N_c^{APB}/N_{tot}^{APB} where N_c^{APB} and N_{tot}^{APB} are the number of conservative APBs and the total number of APBs, respectively, in the microstructure, and an APB between two given APDs is considered as a conservative one if the total length of its conservative segments exceeds that of non-conservative segments; otherwise it is considered as a non-conservative APB. Values of the mean APD size l_d/a in table 1 are rounded to the closest integer.

The results presented in table 1 provide some quantitative characterization of the above-discussed features of evolution. They illustrate, in particular, the predominance of conservative APBs in the microstructures for short-range-interaction systems, particularly at stoichiometric composition $c = 0.25$, as well as a 'freezing' of evolution in such systems due to the virtual immobility of conservative APBs at the not high temperatures under consideration. Table 1 also illustrates a drastic acceleration of evolution under an increase of the interaction range R_{int}, particularly at significant deviations from stoichiometry.

Let us also note that in the above discussion of evolution for different models we considered alloy systems with similar values of concentration c, reduced temperature $T' = T/v_1$, and reduced time $t' = t\gamma_{nn}$. At the same time, the mobility M_{ij} in our main equation (2) has the form $M_{ij} = \gamma_{nn} f\{c_k\}$ where $f\{c_k\}$ is some smooth function of mean occupations c_k (given

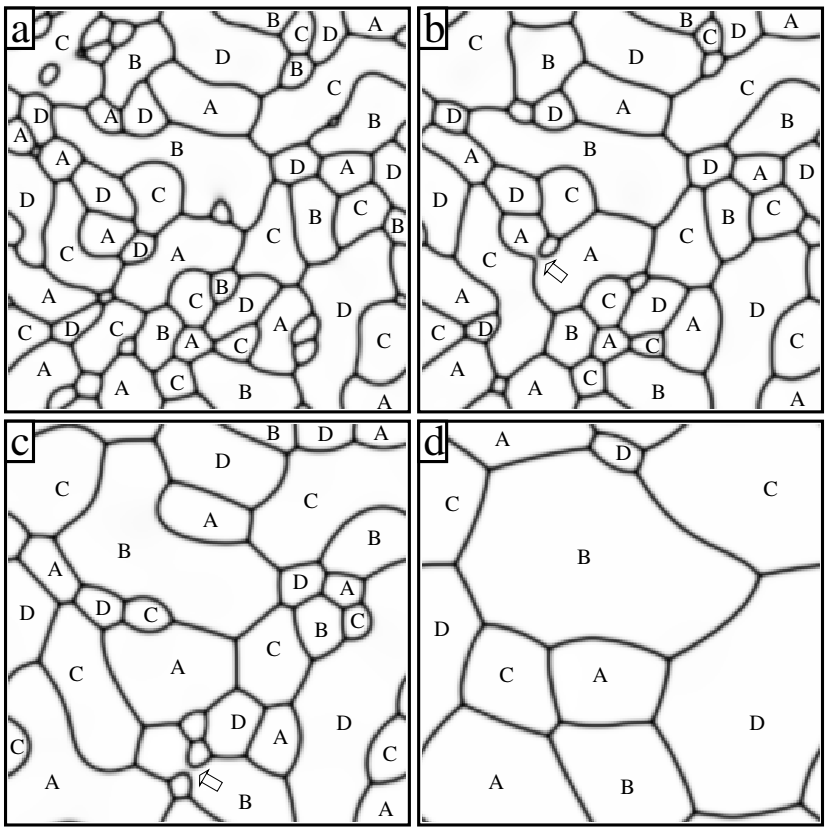

Figure 5. As figure 2, but for model 5 at $T' = T/v_1 = 1.34$, $c = 0.25$, and the following values of t': (a) 10; (b) 20; (c) 50; and (d) 250.

by equation (I.12) in I with $u_i = 0$). Thus in terms of the reduced time t' the kinetic equation (2) has a similar form for all models under consideration. Therefore, the above-discussed differences in the microstructural evolution for different systems are mainly determined by the differences in the non-equilibrium thermodynamic factor $\beta(\lambda_j - \lambda_i)$ in the right-hand side of equations (2), i.e. by the different relations between the thermodynamic driving forces and the local thermodynamic barriers for typical configurations of APBs in the different systems.

Let us discuss the internal structure of APBs in the $L1_2$ phase. Some results of our simulations of this structure are presented in figure 6 where we show the distributions of local concentrations $\overline{c}_i$ and local order parameters $|\eta_{\alpha i}|$ near some approximately (100)-oriented non-conservative APBs for several models and concentrations. In an analysis of the profiles of local order parameters $|\eta_\alpha(x_i)|$ in this figure one should consider that within each $L1_2$-ordered APD all three values $|\eta_\alpha|$ are the same, and within two adjacent APDs separated by the given APB one of parameters η_α (to be denoted as η_l) has the same value, while each of the two others (η_m and η_n) changes its sign on crossing the APB. Therefore, the values $|\eta_m(x_i)|$ and $|\eta_n(x_i)|$ for different APBs can significantly fluctuate depending on the precise location of an APB relative to adjacent crystal planes. Thus it is more convenient to characterize the APB structure by the profiles of the largest order parameter $|\eta_l(x_i)|$ and the local concentration $\overline{c}(x_i)$ in the APB region. In table 2 we present some characteristics of these profiles for non-conservative APBs at reduced times $t' = 200$–250. The quantities η_l^{min} or η_l^{max} and $\overline{c}_{min}$ or

Table 1. Some characteristics of APBs and APDs observed in the simulation of A1 → $L1_2$ and A1 → $L1_0$ transformations.

Simulation box volume $L^2 \times H$	Model	Temperature $T' = T/v_1$	Concentration c	Portion of c-APBs, $v_c = N_c^{APB}/N_{tot}^{APB}$	Number of APDs, N_d			Mean APD size $l_d/a = L/N_d^{1/2}$		
Reduced time of evolution, $t' = t\gamma_{nn}$:				200	10	50	200	10	50	200
A1 → $L1_2$ transition										
$64^2 \times 1$	1	0.35	0.25	0.67	29	28	28	12	12	12
	2	0.5	0.25	0.61	23	17	16	13	16	16
	2	0.5	0.22	0.51	16	13	13	16	18	18
	2	0.5	0.32	0.46	22	14	14	14	17	17
	3	0.77	0.25	0.50	16	12	10	16	18	20
$128^2 \times 1$	4	0.685	0.25	0.27	64	31	20	16	23	29
	4	0.685	0.22	0.03	48	27	13	18	25	36
	4	0.685	0.32	0.15	62	24	12	16	26	37
	5	1.34	0.25	0	56	25	9	17	26	43
A1 → $L1_0$ transition										
$64^2 \times 1$	1	0.35	0.50	0.72	49	49	49	9	9	9
	1	0.35	0.44	0.64	37	23	17	11	13	16
	2	0.5	0.50	0.69	48	39	35	9	10	11
	2	0.5	0.44	0.46	40	28	14	10	12	17
	3	0.8	0.50	0.48	35	21	8	11	14	23
	3	0.8	0.44	0.06	36	16	7	11	16	24
$128^2 \times 1$	4	0.774	0.50	0.18	86	26	13	14	25	36
	4	0.774	0.44	0	81	32	11	14	23	39
	5	1.40	0.50	0	85	29	11	14	24	39
	5	1.40	0.44	0	90	39	16	13	20	32

Table 2. Characteristics of structure of non-conservative APBs under the $L1_2$ ordering. Here η_l^{min} or η_l^{max} and $\overline{c}_{min}$ or $\overline{c}_{max}$ are the minimum or the maximum value of the largest local order parameter $|\eta_l|$ and the local concentration $\overline{c}$, respectively, in the APB region, and δ is the APB width.

		$c = 0.22$			$c = 0.25$			$c = 0.32$		
Model	T'	η_l^{min}	$\overline{c}_{min}$	δ/a	η_l^{min}	$\overline{c}_{min}$	δ/a	η_l^{max}	$\overline{c}_{max}$	δ/a
2	0.5	0.08–0.13	0.15	4–5	0.17–0.21	0.22–0.23	2.5–3	0.33–0.35	0.37–0.38	5–6
4	0.685	0.11–0.12	0.15–0.16	4–5	0.20–0.23	0.23–0.24	2.5–3	0.33–0.35	0.37–0.38	5–6
5	1.34	0.11–0.12	0.15–0.16	4–5	0.17–0.20	0.22–0.23	3–3.5	0.33–0.36	0.37–0.38	5–6

$\overline{c}_{max}$ in this table are the minimum or the maximum value of the largest local order parameter $|\eta_l|$ and the local concentration $\overline{c}$, respectively, in the APB region, and δ is the APB width defined as the distance between the first and the last lattice site for which the $\eta_{\alpha i}$- and c_i-values noticeably differ from those within the ordered domain. The scatter in the parameter η_l^{min}, η_l^{max}, $\overline{c}_{min}$, $\overline{c}_{max}$, or δ for different APBs (as well as for different parts of the same APB) for the given c, T, and model is characterized by the interval of this parameter given in table 2 and is relatively small.

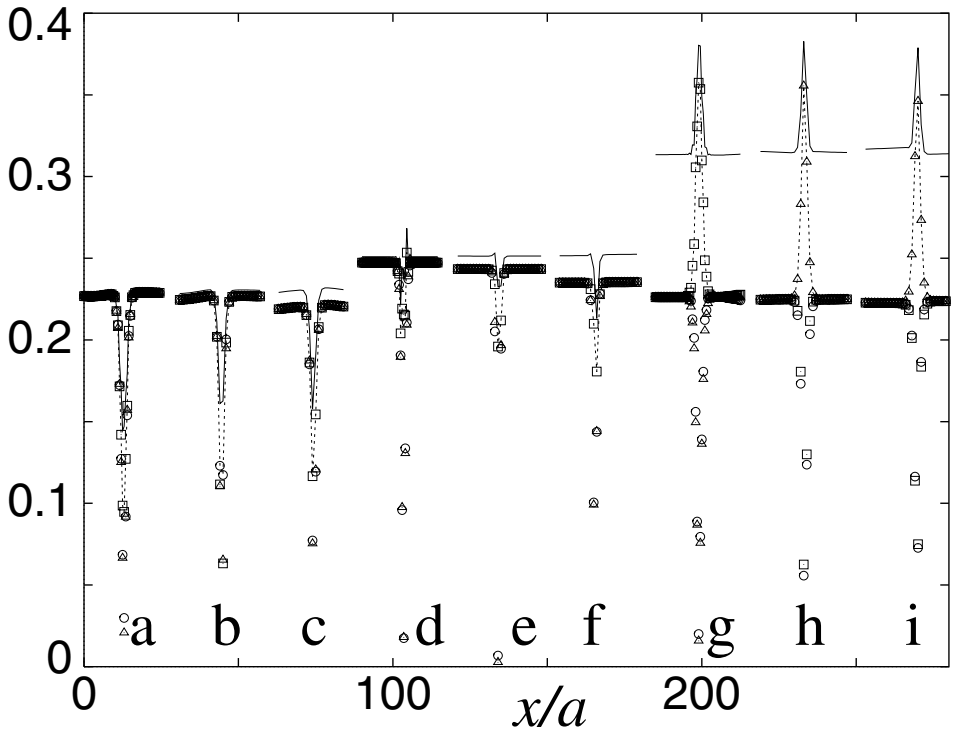

Figure 6. Variation of the local concentration $\overline{c}_i$ and local order parameters $|\eta_{\alpha i}|$ with the coordinate x in the $L1_2$ phase near some approximately (100)-oriented non-conservative APBs. The solid line corresponds to $\overline{c}_i$; triangles, circles, and squares correspond to $|\eta_{1i}|$, $|\eta_{2i}|$, and $|\eta_{3i}|$, respectively; and the dotted line links values of the largest order parameter $|\eta_{li}|$ for clarity. The profiles correspond to the following models, temperatures and concentrations: (a) model 2, $T' = 0.5$, $c = 0.22$; (b) model 4, $T' = 0.685$, $c = 0.22$; (c) model 5, $T' = 1.34$, $c = 0.22$; (d) model 2, $T' = 0.5$, $c = 0.25$; (e) model 4, $T' = 0.685$, $c = 0.25$; (f) model 5, $T' = 1.34$, $c = 0.25$; (g) model 2, $T' = 0.5$, $c = 0.32$; (h) model 4, $T' = 0.685$, $c = 0.32$; and (i) model 5, $T' = 1.34$, $c = 0.32$.

Figure 6 and table 2 show that the concentration dependence of the APB structure in the $L1_2$ phase is very sharp. At lower $c = 0.22$ the local order parameters and local concentrations decrease in the APB region much more sharply than at stoichiometric $c = 0.25$. In contrast, at higher $c = 0.32$ the APB structure manifests a high degree of a local $L1_0$ order: the largest order parameter $|\eta_{li}|$ here considerably exceeds two others, $|\eta_{mi}|$ and $|\eta_{ni}|$, being close to the local concentration $\overline{c}_i$, which corresponds to an 'almost perfect' $L1_0$ ordering. At the same time, the internal structure of APBs seems to be not very sensitive to the interaction type, contrasting greatly with the sharp dependence of the orientation and morphology of APBs on the interaction range R_{int} discussed above. The internal structure of the APB at the given concentration c and temperature T appears to be mainly determined by the location of this c, T point in the equilibrium phase diagram, particularly by the distance Δ between this point and the nearest two-phase region $L1_2$ + X: the smaller Δ, the closer the APB structure to that characteristic of the phase X. In particular, at lower $c = c_- = 0.22$ the 'nearest' phase X is the disordered phase A1 with the equilibrium concentration $c_{A_1} < c_-$, and both the local order parameters $|\eta_{\alpha i}|$ and the local concentration $\overline{c}_i$ within APBs at $c = c_-$ are notably lower than those at stoichiometric $c_s = 0.25$. In contrast, at higher $c = c_+ = 0.32$ the 'nearest'

phase X is the $L1_0$ phase with the equilibrium concentration $c_{L1_0} > c_+$; thus APBs show a significant degree of a local $L1_0$ order with the local concentration $\bar{c}_{max} > c_+$. Analogous structural variations are discussed below for APBs in the $L1_0$ phase near the $L1_0 + L1_2$ two-phase region, while earlier similar variations have been noted for APBs under the B2 [2] and the $D0_3$ [8] ordering. Therefore, such microstructural 'proximity effects' can be a general feature of the APB structure in ordered alloys.

Let us now discuss the fusion-of-domain processes. For the simplest B2 ordering with just two types of ordered domain the only mechanism of microstructural evolution is the growth of larger ordered domains at the expense of smaller ones via motion of APBs separating these domains [1–4]. For multivariant orderings such as the $L1_2$ or $L1_0$ ordering there exists one more mechanism of domain growth, the fusion of different in-phase domains, which can be rather important at not very late stages of evolution. Some examples of such processes can be seen in figures I.7–I.9 in I. Here we discuss this mechanism in more detail.

Figures 2–5 illustrate two possible versions of the fusion-of-domain mechanism.

The first one corresponds to a thinning and a subsequent break of the contact between two adjacent APDs which initially separate the in-phase domains to be fused; for brevity it will be called the 'break-of-contact' (BC) mechanism. It can be followed, for example, in frames 3(c)–3(e) where the lower and the upper A-type domains (A domains) fuse via two sequential breaks of contacts marked by arrows in the lower part of frames 3(d) and 3(e); in frames 5(a)–5(c) where these processes are marked by arrows in frames 5(b) and 5(c); etc.

The second mechanism corresponds to the diminution and the subsequent disappearance of an intermediate domain (or its inner part) that initially separates two in-phase domains to be fused; for brevity it will be called the 'disappearance-of-an-intermediate-domain' (DID) mechanism. It can be followed in frames 3(b)–3(d) where two such processes are marked by arrows in the left and upper part of frame 3(d); in frames 2(a) and 2(b) where this process is marked by an arrow in frame 2(b); etc. The DID mechanism differs from the BC one both topologically and kinetically. First, the number of APDs under the fusion via a DID process is less by unity than before the fusion (or more by unity, if just an inner part of an APD disappears) while for a BC process the number of APDs does not change. Second, the driving force for a DID process is the cumulative thermodynamic gain due to a vanishing of all APBs of an APD, while just a single APB separating two nearby APDs vanishes under a BC process, so its driving force is mainly determined by the surface energy σ of this particular APB. Therefore, the BC processes can be significantly enhanced if APBs with high values of σ, such as the shift-APBs under $L1_0$ ordering discussed below, are present in the system, while the frequency of DID processes is less sensitive to the presence of such APBs.

To more quantitatively characterize the importance of different fusion-of-domain processes under the $A1 \rightarrow L1_2$ transition and to compare it with the $A1 \rightarrow L1_0$ transition, in table 3 we present some data related to the BC and DID processes observed in our simulations. The reduced evolution time t' in this table indicates the time interval (beginning from the initial state at $t' = 5$) for which these processes have been observed. The number N_{BC} or N_{DID} in table 3 is the total number of BC or DID processes observed for each simulation, and N_{tot} is the total number of fusion-of-domain processes. The table shows that the BC and DID-type events under the $A1 \rightarrow L1_2$ transition happen with about the same frequency.

A closer examination of the evolution illustrated by figures 2–5 shows that the fusion-of-domain mechanism is one of main kinetic paths for this evolution. At the same time this mechanism can be realized only in the systems where APBs are mobile, such as our models 4 and 5. In the short-range-interaction systems, such as our models 1 and 2, the APBs are mostly conservative and immobile, the domain growth is mainly realized via the interaction of

Table 3. Statistics of various fusion-of-domain processes observed in the present simulation of A1 → $L1_2$ and A1 → $L1_0$ transformations.

Simulation box volume	Model	T'	c	Reduced time of evolution, t'	Number of events			
A1 → $L1_2$ transition:					N_{DID}	N_{BC}		N_{tot}
$128^2 \times 1$	4	0.685	0.25	150	6	9		15
	4	0.685	0.22	150	6	5		11
	4	0.685	0.32	100	4	8		12
	5	1.34	0.25	150	9	5		14
A1 → $L1_0$ transition:					N_{DID}	$N_{\mathrm{BC}f}$	$N_{\mathrm{BC}s}$	N_{tot}
$64^2 \times 1$	1	0.35	0.50	200	—	—	—	—
	1	0.35	0.44	150	1	3	2	6
	2	0.5	0.50	100	2	2	4	8
	2	0.5	0.44	150	—	3	5	8
	3	0.8	0.50	100	—	4	4	8
	3	0.8	0.44	350	—	4	7	11
$128^2 \times 1$	4	0.774	0.50	150	4	7	8	19
	4	0.774	0.44	400	7	7	14	28
	5	1.40	0.50	300	6	3	16	25
	5	1.40	0.44	350	7	6	11	24

non-conservative and conservative APBs discussed in I and below, and the fusion-of-domain processes are not typical for the evolution.

4. Kinetics of the A1 → $L1_0$ transformation in systems with the short-range interaction

As mentioned, the features of microstructural evolution under the A1 → $L1_0$ transition for alloy systems with the short-range and the extended-range interaction are quite different, just as for the A1 → $L1_2$ transition. In this section we consider this evolution for the short-range-interaction systems. To this end we discuss the results of our simulations for the second-neighbour interaction models 1, 2, and 3 mentioned in section 2.

Some results of these simulations are presented in figures 7–11. The label A or $\overline{\mathrm{A}}$ in these figures corresponds to an $L1_0$-ordered domain with the tetragonal axis c along (100) and the positive or negative value, respectively, of the order parameter η_1; the label B or $\overline{\mathrm{B}}$ corresponds to that for the c-axis along (010) and the order parameter η_2; and the label C or $\overline{\mathrm{C}}$ corresponds to that for the c-axis along (001) and the order parameter η_3. Frame 7(c) shown in the c-representation illustrates the occupation of lattice sites for each domain type.

A distinctive feature of the microstructures shown in figures 7–11 is a predominance of conservative APBs with (100)-type orientation, particularly for models 1 and 2 at stoichiometric composition $c = 0.5$. For the nearest-neighbour-interaction model with $v_{n>1} = 0$ at $c = 0.5$ such APBs have a zero excess energy, just like analogous conservative APBs under the $L1_2$ ordering [6,7]; thus for models 1 and 2 with small $|v_2/v_1|$ this excess energy is small. There are two types of conservative APB for the $L1_0$ ordering: the conservative shift-type APB (c-shift APB), and the conservative flip-type APB (c-flip APB). The microscopical structure of these APBs is illustrated in frame 7(c). Figures 7–11 show that the thickness of a c-shift APB in the η^2-representation is about twice as large as that of a c-flip APB; this facilitates an analysis of microstructures in figures 7–11. A consideration of possible orientations of conservative

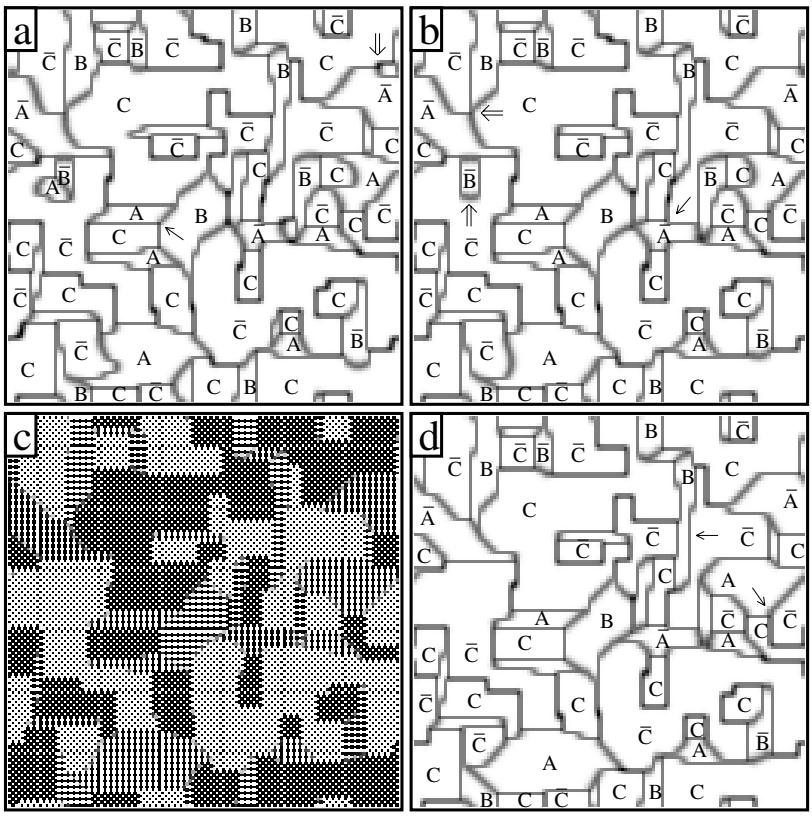

Figure 7. Temporal evolution of the second-neighbour-interaction model 1 with $\epsilon = v_2/v_1 = -0.125$ under the phase transformation A1 $\rightarrow$ $L1_0$ for the simulation box size $V_b = 64^2 \times 1$ at $T' = T/v_1 = 0.35$, $c = 0.5$, and the following values of t': (a) 5; (b) 10; (c) 50; and (d) 200. Frame (c) is shown in the c-representation with the grey level linearly varying with c_i between its minimum and maximum values from completely dark to completely bright, and the rest of the frames are shown in the η^2-representation. The label A, $\overline{\text{A}}$, B, $\overline{\text{B}}$, C, or $\overline{\text{C}}$ indicates the type of the ordered domain as described in the text. The single and the double arrows here and below indicate the characteristic configurations and the characteristic kinetic processes, respectively, for the microstructures with conservative APBs discussed in the text.

APBs in the $L1_0$ phase shows that the plane of a c-shift APB separating the APDs with the same tetragonal axis should be parallel to this axis, while the plane of a c-flip APB separating two APDs with perpendicular tetragonal axes should be parallel to both these axes. For quasi-2D microstructures with edge-on APBs shown in figures 7–11 this implies that a c-shift APB separating APDs A and $\overline{\text{A}}$ (c-APB A–$\overline{\text{A}}$) is horizontal; c-APBs B–$\overline{\text{B}}$ are vertical; and c-APBs C–$\overline{\text{C}}$ can be both horizontal and vertical; a c-flip APB (A or $\overline{\text{A}}$)–(C or $\overline{\text{C}}$) (which separates APDs A or $\overline{\text{A}}$ from C or $\overline{\text{C}}$) is horizontal; c-APBs (B or $\overline{\text{B}}$)–(C or $\overline{\text{C}}$) are vertical; and c-APBs (A or $\overline{\text{A}}$)–(B or $\overline{\text{B}}$) should lie in the plane of figure and thus they are not seen in figures 7–11.

The conservative APBs in figures 7–11 are notably thinner than non-conservative ones, particularly for flip-APBs. The figures also show that the mobility of conservative APBs is quite low, and the growth of ordered domains is mainly realized via motion of non-conservative APBs, just as for the $L1_2$ ordering [7].

Models 2 and 3 correspond to a larger interaction range than model 1. Therefore, the energetic preference (and hence the predominance in the microstructures) of conservative

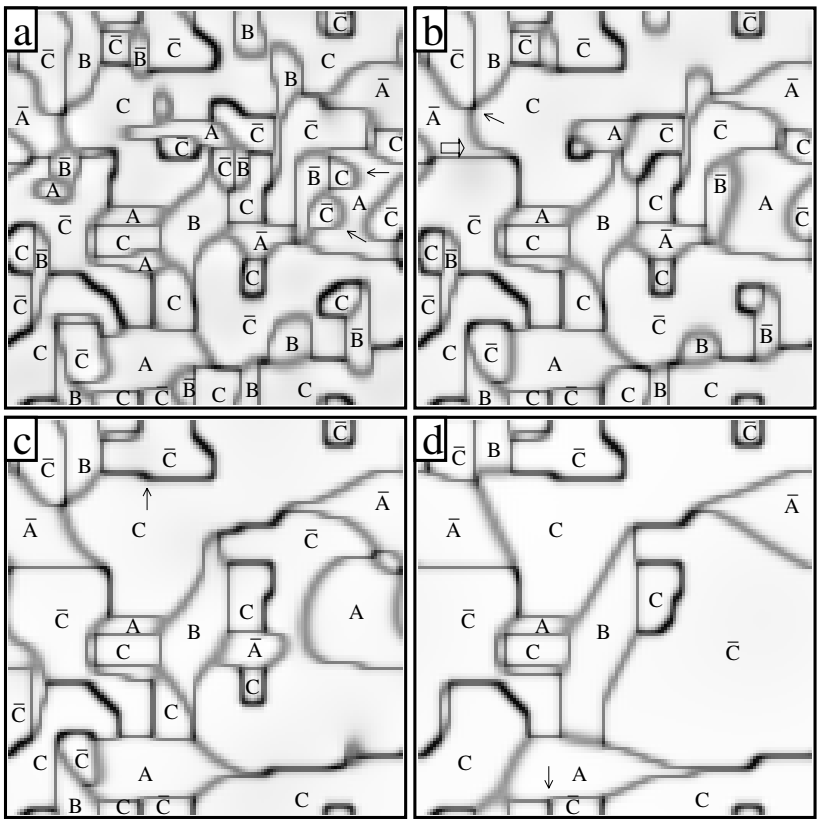

Figure 8. As figure 7, but at $c = 0.44$ and shown in the η^2-representation.

APBs with respect to non-conservative APBs for model 2 is less pronounced than for model 1, and it is still less for model 3. The reduction in the number of low-mobility conservative APBs leads to an acceleration of evolution. All these features are illustrated by figures 7, 9, and 11, and they are analogous to those observed in I for the A1 $\rightarrow$ $L1_2$ transition. However, the concentration dependence of the evolution (which is illustrated by comparison of figures 7 with 8 and 9 with 10) is here sharper than that under the A1 $\rightarrow$ $L1_2$ transition. This implies that the energetic preference of conservative APBs in the $L1_0$ phase decreases with the deviation from stoichiometry much more rapidly than that in the $L1_2$ phase. In particular, the microstructures for model 2 at off-stoichiometric $c = 0.44$ shown in frames 10(a)–10(d) reveal a much more isotropic distribution of APBs and a higher evolution rate than those at stoichiometric $c = 0.5$ shown in frames 9(a)–9(d), while the microstructures for model 3 at $c = 0.44$ (not shown in this paper for reasons of space) include almost no conservative APBs, unlike those at $c = 0.5$ shown in figure 11. This greatly differs from the relatively weak concentration dependence of the evolution under the A1 $\rightarrow$ $L1_2$ transition illustrated by figure 1. All these features of evolution are illustrated by values ν_c, $N_d(t')$, and $l_d(t')$ for models 1, 2, and 3 under the A1 $\rightarrow$ $L1_0$ transition in table 1, and these values can be compared with those for the A1 $\rightarrow$ $L1_2$ transition in the upper part of this table.

In the discussion of simulations of the A1 $\rightarrow$ $L1_2$ transformation for the short-range-interaction systems in paper I we noted a number of microstructural features which agree well with experimental observations for such systems, in particular, for the Cu_3Au alloy [19, 20].

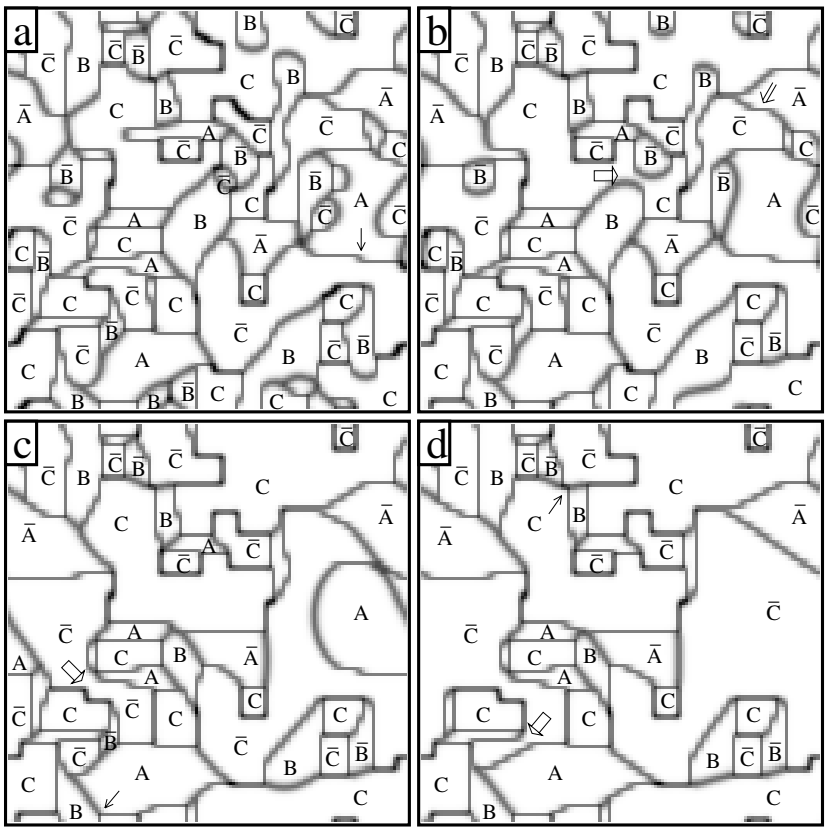

Figure 9. As figure 8, but for model 2 with $\epsilon = -0.25$ at $T' = 0.5$, $c = 0.5$, and the following values of t': (a) 5; (b) 12; (c) 50; and (d) 200.

Below we list the analogous features for the A1 $\rightarrow$ $L1_0$ transition observed in the present simulation:

(i) The predominance of conservative APBs with (100)-type orientation.
(ii) The presence of both shift and flip-type APBs with slight deviation from the (100) plane which actually have a step-like, 'facetted' structure with long conservative steps and small non-conservative ledges normal to these steps.
(iii) The presence of triple junctions of APBs that include three or two conservative APBs which are either normal or parallel to each other.
(iv) The presence of loop-like configurations of some non-conservative APBs adjacent to the conservative APBs.
(v) The presence of quadruple junctions of APDs of the type $A_1A_2\overline{A_1}A_3$ where A_2 and A_3 can correspond to any two of the four types of APD different from A_1 and $\overline{A_1}$.

The microstructures shown in figures 7–11 illustrate all these observations. Point (i) has been already discussed above. As examples of facetted APBs mentioned in point (ii) one can note approximately horizontal ('quasi-horizontal') shift-APBs $\overline{C}$–C marked by an arrow in frames 8(c) and 10(d); a quasi-vertical flip-APB B–$\overline{C}$ marked by an arrow in the upper right part of frame 7(d); quasi-horizontal flip-APBs A–$\overline{C}$ marked by an arrow in frames 9(a) and 11(f); etc. The triple junctions mentioned in point (iii) can join APBs of the following types:

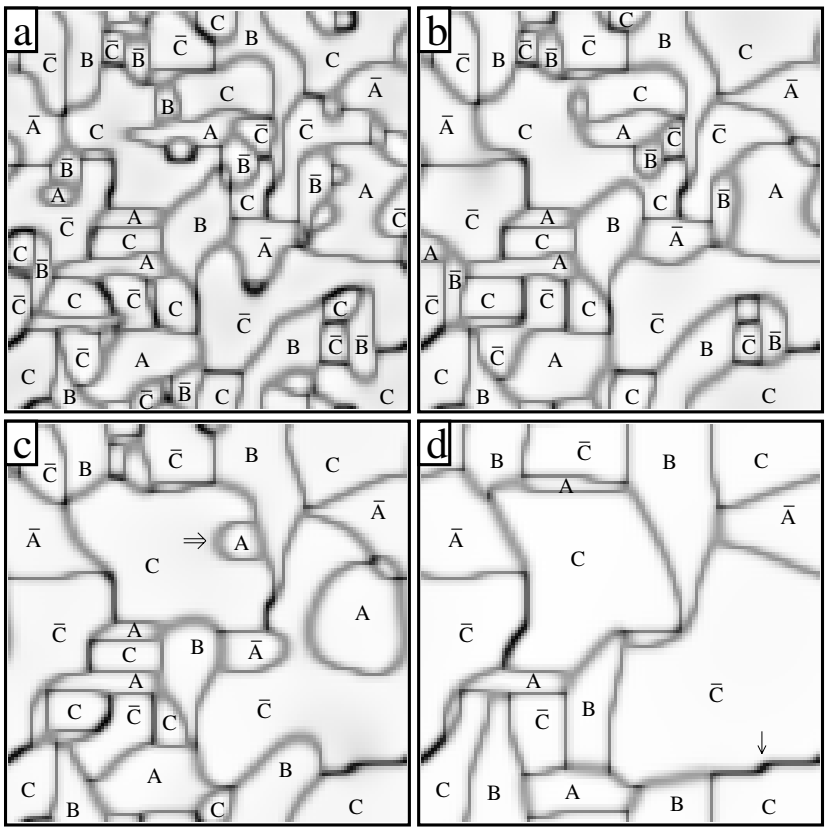

Figure 10. As figure 9, but at $c = 0.44$ and the following values of t': (a) 5; (b) 20; (c) 50; and (d) 200.

(a) two conservative flip-APBs and a conservative shift-APB, as, for example, in the junctions $CA\overline{C}$ and $C\overline{C}\,\overline{A}$ marked by a single arrow in frames 7(b) and 8(d);

(b) two conservative flip-APBs normal to each other and a non-conservative APB, as in the junctions ABC and BAC marked by a single arrow in frames 7(a) and 9(c); and

(c) a conservative shift-APB, a conservative flip-APB, and a non-conservative flip-APB, as in the junctions $A\overline{C}C$ and $\overline{A}C\overline{C}$ marked by an arrow in the right-hand central part of frame 7(d) and in frame 11(d).

Examples of loop-like APDs adjacent to conservative APBs mentioned in point (iv) can be: APDs C and $\overline{C}$ marked by arrows in frame 8(a); a domain $\overline{B}$ marked by a single arrow in frame 11(a); etc. As examples of quadruple junctions mentioned in point (v) one can note the junctions $\overline{C}BC\overline{A}$, $\overline{B}\,\overline{C}BC$ and $\overline{A}CB\overline{C}$, marked by a single arrow in frames 8(b), 9(d), and near the centre of frame 11(f), respectively; etc. Let us also note that the quadruple junctions mentioned in point (v), unlike other configurations (i)–(iv), are characteristic not only for the short-range-interaction systems, but still more so for the systems with a larger interaction range to be discussed below.

Let us now discuss the kinetics of the $A1 \rightarrow L1_0$ transition for short-range-interaction systems. As mentioned, evolution in such systems is realized via motion of non-conservative APBs and their interaction with conservative APBs. The mechanisms of this interaction are

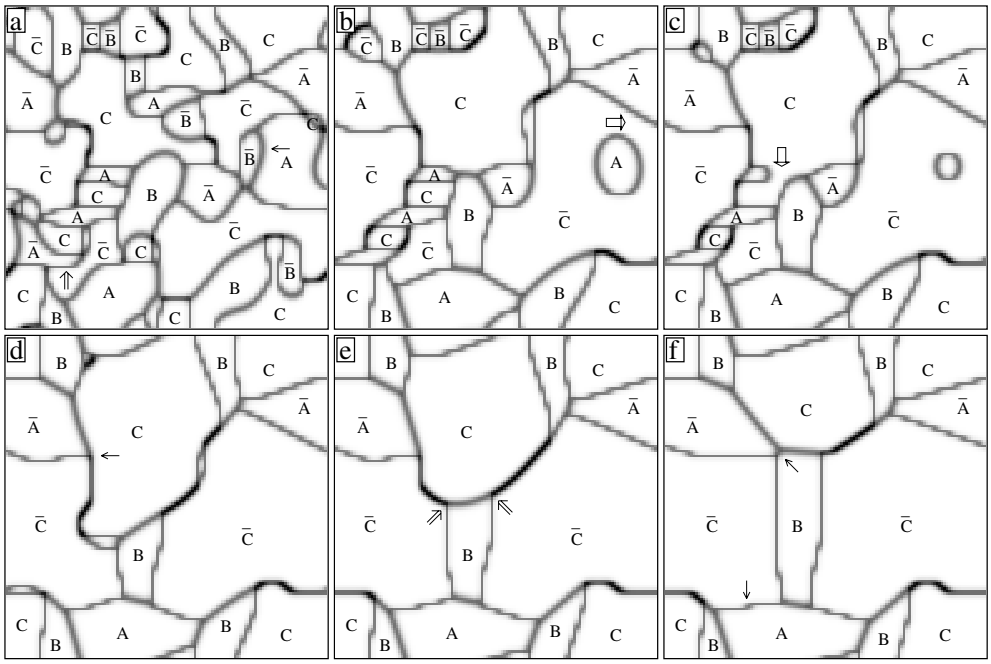

Figure 11. As figure 9, but for model 3 with $\epsilon = -0.5$ at $T' = 0.8$, $c = 0.5$, and the following values of t': (a) 10; (b) 50; (c) 60; (d) 100; (e) 200; and (f) 500.

analogous to those discussed in I for the A1 $\rightarrow$ $L1_2$ transition. In particular, 'sweeping' of a conservative APB (c-APB) by an adjacent moving non-conservative APB (nc-APB) mentioned in I can be seen in frames 7(b), 7(c) and 9(b), 9(c) where an nc-APB $\overline{\text{C}}$–B marked by a vertical double arrow in frame 7(b) sweeps two vertical c-APBs; above the centre of frames 10(c), 10(d) where an nc-APB C–A marked by a horizontal double arrow in frame 10(c) sweeps two horizontal c-APBs; etc. 'Wetting of a c-APB by adjacent nc-APBs' can be seen in frames 9(b)–9(d) where a horizontal conservative segment of an APB $\overline{\text{A}}$–$\overline{\text{C}}$ marked by a double arrow in frame 9(b) is wetted by adjacent non-conservative segments (which eventually leads to a straightening of this APB in frame 9(d)); in frames 11(a), 11(b) where a conservative horizontal segment of an APB $\overline{\text{A}}$–$\overline{\text{C}}$ (marked by a double arrow in frame 11(a)) is wetted, too; etc. 'Motion of a triple junction of two nc-APBs with a c-APB along the direction of the latter' discussed in I is seen in frames 7(a), 7(b) where a horizontal c-APB C–$\overline{\text{A}}$ 'pushes' the triple junction marked by a double arrow in frame 7(a) to the right up to the crossing of a vertical c-APB; below the centre of frames 11(e), 11(f) where two triple junctions of vertical c-APBs marked by double arrows in frame 11(e) move up until the formation of their triple junctions with horizontal c-APBs; etc. Finally, 'splitting of an nc-APB into a c-APB and an nc-APB' can be seen in the upper left corner of frames 7(a)–7(d) where non-conservative segments of APBs marked by a horizontal double arrow in frame 7(a) are split into two vertical conservative segments.

In addition to the four above-mentioned kinetic mechanisms, figures 7–11 illustrate the presence of the fusion-of-domain processes analogous to those discussed in section 3 for the A1 $\rightarrow$ $L1_2$ transition. As mentioned, these processes are typical for systems with mobile APBs and are not manifested, for example, for model 1 at stoichiometric $c = 0.5$ in figure 7. However, in the systems with a larger interaction range or at significant deviations from stoichiometry the fusion of domains plays a significant role in evolution. In particular, the DID-type processes

discussed in section 3 can be seen in frames 9(b)–9(d) where this process is marked by a thick arrow in frames 9(d) and 9(c) and corresponds to the disappearance of a domain $\overline{\mathrm{B}}$ and an inner part of a domain A, respectively. The fusion via a break of a flip-APB (to be abbreviated as a BCf process) is illustrated in frames 8(a), 8(b) and 11(b), 11(c) where this process is marked by a thick arrow in frames 8(b) and 11(c). Finally, the fusion via a break of a shift-APB (to be abbreviated as a BCs process) can be followed in frames 9(a), 9(b) and 11(a), 11(b) where this process is marked by a thick arrow in frames 9(b) and 11(b) and corresponds to the break of a shift-APB formed after a disappearance of a domain $\overline{\mathrm{C}}$ and C, respectively.

The relative frequency of various fusion-of-domain processes observed in our simulations can be characterized by the numbers of fusion events via various mechanisms, N_{DID}, $N_{\mathrm{BC}f}$, and $N_{\mathrm{BC}s}$, which are presented in table 3. The table shows, in particular, that the number $N_{\mathrm{BC}s}$ usually notably exceeds $N_{\mathrm{BC}f}$, i.e. the shift-APBs are split more frequently than the flip-APBs, particularly at significant deviations $\delta c = 0.5 - c$ from stoichiometry or at large R_{int}. This reflects a decrease of stability of shift-APBs with respect to flip-APBs under an increase of δc or R_{int} which is discussed in more detail in the next section.

The structure of APBs in the $\mathrm{L1}_0$ phase is illustrated by figure 12. In an analysis of the distribution of local order parameters $|\eta_\alpha(x_i)|$ near APBs in this figure one should consider that after a crossing of a shift-APB the non-zero parameter η_α changes its sign, while after a crossing of a flip-APB it is replaced by another one, η_β, with $\beta \neq \alpha$ but $|\eta_\beta| = |\eta_\alpha|$. In the APB region all three local order parameters η_{1i}, η_{2i}, and η_{3i} are non-zero; thus one can discuss a degree of a local $\mathrm{L1}_0$- or $\mathrm{L1}_2$-type order in this region. The parameters of this local order for systems under consideration with a tendency to either $\mathrm{L1}_0$ or $\mathrm{L1}_2$ ordering can be defined in terms of parameters $\eta_{\alpha i}$ and $\overline{c}_i$ from (5), for example, as follows:

$$\eta_i^{\mathrm{L1}_2} = |\eta_{1i}\eta_{2i}\eta_{3i}|^{1/3}/\overline{c}_i \qquad \eta_i^{\mathrm{L1}_0} = (\eta_{1i}^2 + \eta_{2i}^2 + \eta_{3i}^2 - 3|\eta_{1i}\eta_{2i}\eta_{3i}|^{2/3})^{1/2}/\overline{c}_i. \tag{6}$$

Under a perfect $\mathrm{L1}_2$ ordering we have: $|\eta_1| = |\eta_2| = |\eta_3| = c$, thus $\eta_i^{\mathrm{L1}_2} = 1$, and $\eta_i^{\mathrm{L1}_0} = 0$; while under a perfect $\mathrm{L1}_0$ ordering with a single non-zero $|\eta_\alpha| = c$ we obtain: $\eta_i^{\mathrm{L1}_2} = 0$, and $\eta_i^{\mathrm{L1}_0} = 1$. Therefore, the definition (6) can reasonably characterize a degree of the local $\mathrm{L1}_0$ or $\mathrm{L1}_2$ order in the APB region.

Figure 12 shows the distribution of quantities $\eta_{\alpha i}$, $\overline{c}_i$, $\eta_i^{\mathrm{L1}_0}$, and $\eta_i^{\mathrm{L1}_2}$ near some typical non-conservative APBs for models 2 and 4. The figure also illustrates a strong concentration dependence of the APB structure in the $\mathrm{L1}_0$ phase analogous to that for the $\mathrm{L1}_2$ phase discussed in section 3. In particular, the variations of local concentration $\overline{c}_i$ near APBs at stoichiometric $c = 0.5$ are almost indistinguishable, but at off-stoichiometric $c = 0.44$ the $\overline{c}_i$-values within APBs are notably depleted. The decrease of the $\mathrm{L1}_0$ order parameter $\eta_i^{\mathrm{L1}_0}$ and an increase of the $\mathrm{L1}_2$ order parameter $\eta_i^{\mathrm{L1}_2}$ in the APB region at $c = 0.5$ are relatively weak, but at $c = 0.44$ they are quite pronounced, particularly for the flip-type APBs. These compositional changes can be viewed as one more manifestation of the microstructural 'proximity effect' mentioned in section 3. For both models 2 and 4 the c, T point corresponding to $c = 0.44$ is close to the two-phase region $\mathrm{L1}_0 + \mathrm{L1}_2$ of the phase diagram; thus the APB structure in the single-phase $\mathrm{L1}_0$ region displays the features characteristic of the 'nearby positioned' $\mathrm{L1}_2$ phase.

5. Kinetics of the A1 → $\mathrm{L1}_0$ transition in systems with the intermediate or extended interaction range

As mentioned, models 4 and 5 can be considered as representatives of systems with an intermediate and extended interaction range, respectively. Therefore, simulations of the A1 → $\mathrm{L1}_0$ transition for these models can illustrate the transformation kinetics for such

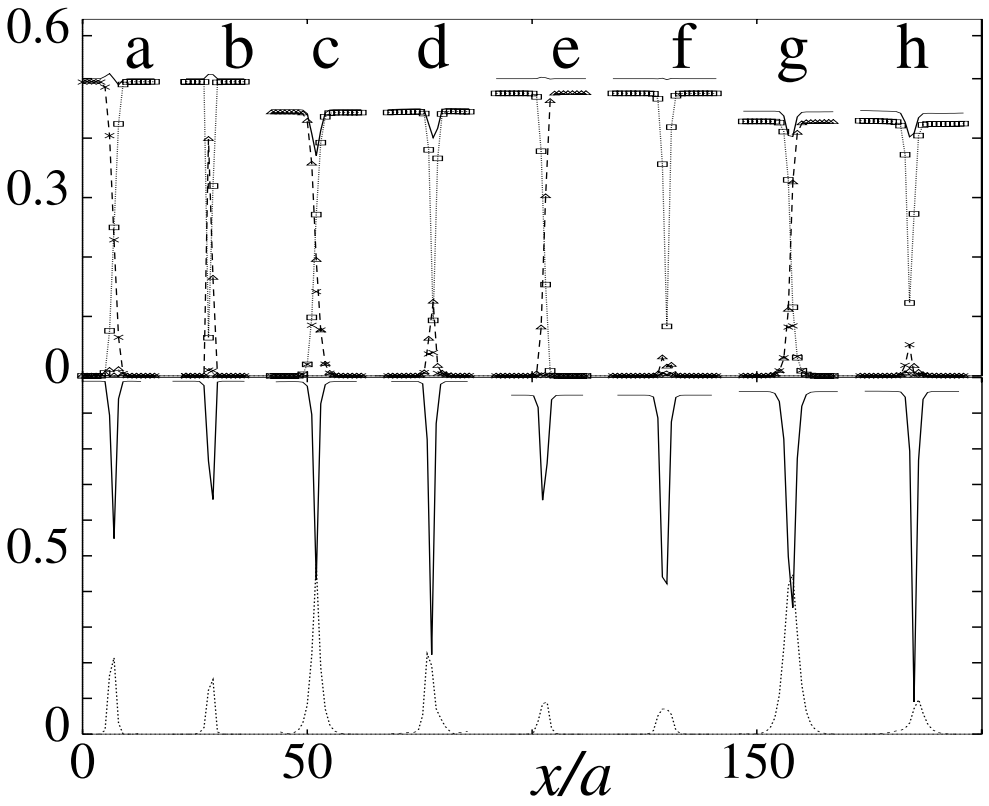

Figure 12. Upper row: variation of the local concentration $\overline{c}_i$ and local order parameters $|\eta_{\alpha i}|$ with the coordinate x in the $L1_0$ phase near some approximately (100)-oriented non-conservative APBs. The solid line corresponds to $\overline{c}_i$; triangles, crosses, and rectangles correspond to $|\eta_{1i}|$, $|\eta_{2i}|$, and $|\eta_{3i}|$, respectively; and dashed or dotted lines link values of two largest order parameters $|\eta_{\alpha i}|$ in the APB region for clarity. The profiles (a)–(d) correspond to model 2 at $T' = 0.5$, and profiles (e)–(h) to model 4 at $T' = 0.774$, for the following APB types and concentrations: (a) and (e), flip-APB at $c = 0.5$; (b) and (f), shift-APB at $c = 0.5$; (c) and (g), flip-APB at $c = 0.44$; and (d) and (h), shift-APB at $c = 0.44$. Lower row: as in the upper row but for the parameters $\eta_i^{L1_0}$ and $\eta_i^{L1_2}$ of the local $L1_0$ or $L1_2$ order defined in the text; the solid line corresponds to $\eta_i^{L1_0}$, and the dotted line to $\eta_i^{L1_2}$.

systems. Some results of these simulations are presented in figures 13–17. Comparing them with figures 7–10 we again see sharp microstructural differences between the systems with different interaction ranges. Unlike in figures 7–10, some conservative APBs are present only in figure 13 for model 4 at stoichiometric concentration $c = 0.5$, while at larger R_{int} or at off-stoichiometric $c = 0.44$ all APBs in the microstructures shown in figures 13–16 are non-conservative. This is similar to the case of the A1 $\rightarrow$ $L1_2$ transition illustrated by figures 2–5. The presence of low-mobility conservative APBs leads to a decrease of the evolution rate relative to those for the systems with just non-conservative APBs; in particular, the total number N_d of different APDs for the scenarios illustrated by figures 13, 14, 15, and 16 at $t' = 400$ is 9, 5, 6, and 6, and l_d/a is 43, 57, 52, and 52, respectively. Some other characteristics of evolution under the A1 $\rightarrow$ $L1_0$ transition for models 4 and 5 are given in the lower part of table 1; they are similar to those under the A1 $\rightarrow$ $L1_2$ transition for same models presented in the upper part of this table.

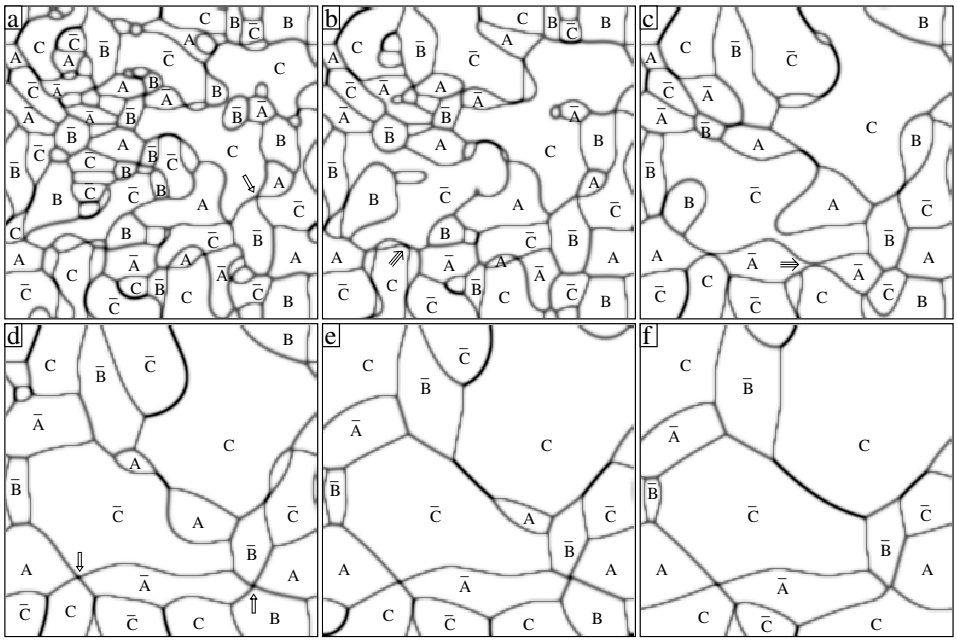

Figure 13. As figure 11, but for model 4 with $V_b = 128^2 \times 1$ at $T = 1300$ K, $c = 0.5$, and the following values of t': (a) 10; (b) 20; (c) 50; (d) 100; (e) 200; and (f) 300. The thin and the triple arrows here and below indicate the quadruple junctions and the processes of splitting of APBs, respectively, discussed in the text.

Another common feature of evolution under the A1 $\rightarrow$ L1$_0$ and A1 $\rightarrow$ L1$_2$ transitions is the presence of the fusion-of-domain processes discussed in sections 3 and 4. The relative frequency of various mechanisms for such fusion is characterized by the numbers of fusion events of a different type in table 3. These numbers show, in particular, that the BC-type processes under the A1 $\rightarrow$ L1$_0$ transition happen more frequently than under the A1 $\rightarrow$ L1$_2$ transition, mainly due to the intense processes of splitting of shift-APBs under the L1$_0$ ordering discussed below.

In addition to the features mentioned above and analogously to those observed for the A1 $\rightarrow$ L1$_2$ transition, figures 13–17 reveal the presence of some peculiar configurations and processes specific for the A1 $\rightarrow$ L1$_0$ transformation.

First, there are the quadruple junctions (4-junctions) $A_1A_2\overline{A_1}A_3$ which are long-living transient configurations which seem to correspond to some local minima in the configurational alloy energy. Such junctions have already been mentioned above in the discussion of models 1, 2, and 3, but for the systems with a larger interaction range they are much more typical. In our simulations we observed two types of such 4-junctions.

(a) Those of a type $A_1A_2\,\overline{A_1}\,\overline{A_2}$ which are particularly stable and are preserved unless some of the four APDs entering the junction disappear; for brevity they will be called 'stable' 4-junctions.

(b) Those of a type $A_1A_2\overline{A_1}A_3$ with $A_3 \neq \overline{A_2}$ which can also be slightly split into two triple junctions with the formation of a short flip-APB but not a shift-APB; for brevity they will be called 'metastable' 4-junctions.

Examples of both stable and metastable 4-junctions in figures 13–17 are numerous. As examples of stable 4-junctions one can note: $A\overline{C}\,\overline{A}C$ and $\overline{A}\,\overline{B}AB$ marked by arrows in frames

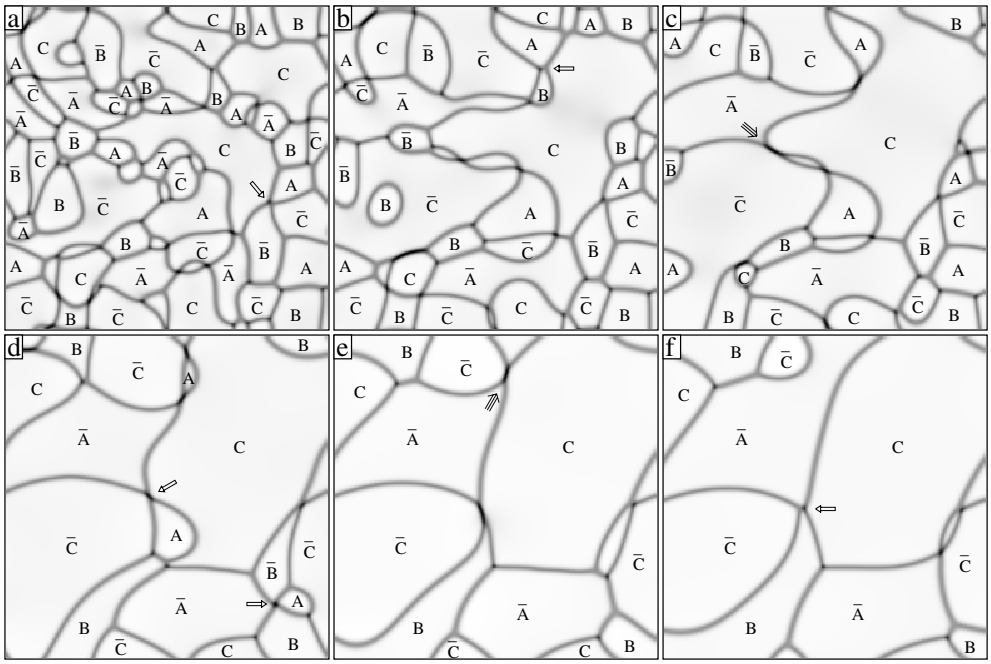

Figure 14. As figure 13, but at $c = 0.44$ and the following values of t': (a) 20; (b) 50; (c) 100; (d) 200; (e) 300; and (f) 400.

13(d) and 14(d); AB$\overline{\text{A}}\,\overline{\text{B}}$ marked by an arrow in frame 16(a); etc. In frames 15(a)–15(c) one can also see a peculiar process of a 'drift' of a stable 4-junction AC$\overline{\text{A}}\,\overline{\text{C}}$ marked by an arrow in frame 15(a) which illustrates a significant stability of this configuration in the course of the evolution. As examples of metastable 4-junctions one can mention: CA$\overline{\text{C}}\,\overline{\text{B}}$ marked by an arrow in frames 13(a) and 14(a) (while in frames 15(a) and 16(a) this junction is already split into two 3-junctions); $\overline{\text{C}}$ACB and $\overline{\text{C}}\,\overline{\text{A}}$CB marked by arrows in frames 14(b) and 14(f); etc.

The other characteristic feature illustrated by figures 13–17 is the presence of numerous processes of splitting of a shift-APB into two flip-APBs. This reflects a decrease of stability of shift-APBs relative to flip-APBs under an increase of the interaction range R_{int} or the deviations δc from stoichiometry. Under a further evolution such splitting can lead to either a fusion of in-phase domains (BCs process) or a formation of a stable or metastable 4-junction ('$s \rightarrow 4j$-process'). The splitting with the domain fusion can be followed, for example, in frames 13(a)–13(d) where an APB $\overline{\text{C}}$–C marked by an arrow in frame 13(c) and formed after the disappearance of a domain A splits with the fusion of two domains $\overline{\text{A}}$; in frames 14(d)–14(f) where an APB $\overline{\text{C}}$–C marked by an arrow in frame 14(e) and formed after a disappearance of a domain A splits with the fusion of domains $\overline{\text{A}}$; in frames 15(a), 15(b) and 16(b), 16(c) where an APB A–$\overline{\text{A}}$ marked by an arrow in frames 15(a) and 16(b) and formed after the disappearance of a domain $\overline{\text{C}}$ splits with the fusion of two domains C; etc. The $s \rightarrow 4j$-process can be followed: in frames 13(b)–13(d) where an APB $\overline{\text{C}}$–C marked by an arrow in frame 13(b) and first increasing its length due to the disappearance of several small APDs splits with the formation of a 4-junction A$\overline{\text{C}}\,\overline{\text{A}}$C; in frames 14(c), 14(d) where an APB $\overline{\text{C}}$–C marked by an arrow in frame 14(c) splits with the formation of a 4-junction $\overline{\text{C}}\,\overline{\text{A}}$CA; in frames 15(b)–15(d) where an APB C–$\overline{\text{C}}$ marked by an arrow in frame 15(b) splits with the formation of a 4-junction CA$\overline{\text{C}}\,\overline{\text{B}}$; etc.

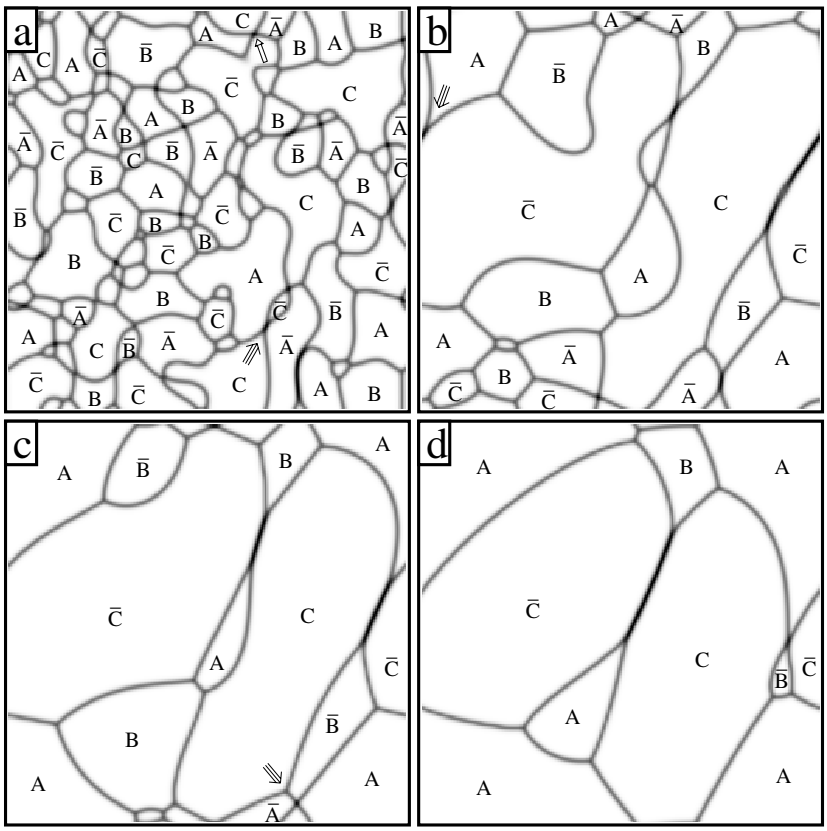

Figure 15. As figure 13, but for model 5 at $T' = 1.4$, $c = 0.5$, and the following values of t': (a) 10; (b) 100; (c) 200; and (d) 400.

The processes of splitting of shift-APBs become particularly pronounced at significant deviations from stoichiometry. In particular, at $c = 0.44$ one can observe few shift-APBs in figure 14 and almost none of them in figure 16 as each shift-APB formed in the course of the evolution splits into flip-APBs shortly after its formation. The stability or metastability of the 4-junctions mentioned above is also related to a high excess energy of a shift-APB which makes the decay of such a junction with the formation of a shift-APB energetically unfavourable.

Among other kinetic processes observed in this simulation one can mention a peculiar 'collision' of a triple and a quadruple junction seen in frames 15(c), 15(d) which happens due to a break of a flip-APB $\overline{\mathrm{C}}$–$\overline{\mathrm{B}}$ marked by an arrow in frame 15(c). The resulting 5-junction $\overline{\mathrm{A}}\mathrm{C}\overline{\mathrm{B}}\mathrm{AB}$ almost immediately (for $\delta t' \sim 1$) splits into three 3-junctions, $\mathrm{CB}\overline{\mathrm{A}}$, CAB, and $\mathrm{C}\overline{\mathrm{B}}\mathrm{A}$, with the formation of two flip-APBs.

In figure 17 we present some results of a 3D simulation with $V_b = 50^3$ for model 5 at $c = 0.5$. This simulation aimed mainly at a comparison with 2D simulations; thus it was performed only for a limited time interval $t' \lesssim 20$. Comparison of figures 17 and 13–16 illustrates some differences between 3D and 2D microstructures, in particular, the presence in 3D microstructures of 'checkered' regions. These regions correspond to the parts of APBs (with significant values of the derivative $\mathrm{d}\eta_3/\mathrm{d}z$ [7]) which lie approximately in the plane of figure, while in 2D microstructures only the edge-on APBs are presented. Besides, some 3D APBs in figure 17 are tilted to the plane of figure and thus they seem to be thicker than the

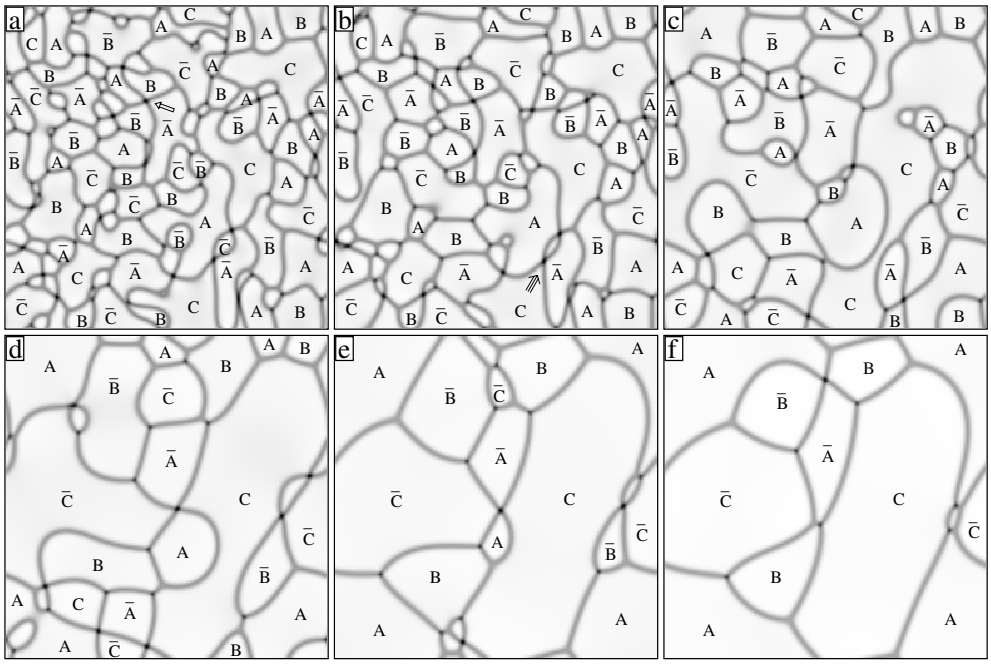

Figure 16. As figure 15, but at $c = 0.44$ and the following values of t': (a) 10; (b) 20; (c) 50; (d) 120; (e) 300; and (f) 450.

edge-on APBs shown in figures 13–16. However, all main features of evolution discussed above for the 2D microstructures are also present in 3D simulation. In particular, the fusion-of-domain processes (marked by thick arrows) can be seen: in frames 17(a), 17(b) where two A domains fuse after the disappearance of a minor domain $\overline{\mathrm{C}}$ and C, respectively; in the upper left part of frames 17(d), 17(e) where an APB $\overline{\mathrm{A}}$–B breaks with the fusion of two domains C; in the left-hand upper part of frames 17(b), 17(c) where an APB $\overline{\mathrm{A}}$–A splits with the fusion of two domains $\overline{\mathrm{B}}$; in the right-hand central part of frames 17(d)–17(f) where an APB $\overline{\mathrm{B}}$–B splits with the fusion of two domains $\overline{\mathrm{B}}$; etc. Frames 17(a)–17(f) also show the presence of many 4-junctions (marked by thin arrows), such as $\mathrm{A}\overline{\mathrm{B}}\,\overline{\mathrm{A}}\mathrm{B}$, $\overline{\mathrm{B}}\mathrm{A}\mathrm{B}\overline{\mathrm{A}}$, and $\overline{\mathrm{A}}\mathrm{A}\mathrm{B}\overline{\mathrm{B}}$ in frame 17(a); $\mathrm{C}\overline{\mathrm{B}}\,\overline{\mathrm{C}}\mathrm{B}$ in frame 17(e); $\mathrm{B}\overline{\mathrm{C}}\,\overline{\mathrm{B}}\mathrm{C}$ in frame 17(f); etc. The $s \to 4j$-processes (marked by triple arrows) can be seen in frames 17(d)–17(f) where an APB C–$\overline{\mathrm{C}}$ splits with the formation of a 4-junction $\mathrm{C}\overline{\mathrm{B}}\,\overline{\mathrm{C}}\mathrm{B}$ while an APB $\overline{\mathrm{B}}$–B splits with the formation of a 4-junction $\overline{\mathrm{B}}\mathrm{C}\mathrm{B}\mathrm{A}$; etc. The lower right part of frames 17(a)–17(c) also illustrates a splitting of a shift-APB $\overline{\mathrm{B}}$–B accompanied by the growth of a domain C (which was initially located above the plane of frames 17(a)–17(c)) in the direction z normal to the plane of figure. Therefore, the main features of the microstructure under 2D and 3D simulations appear to be the same, which justifies the use of 2D simulations for studies of these features.

The structure of APBs in the $L1_0$ phase for model 4 is illustrated by the distributions of local order parameters and local concentrations presented in the right-hand part of figure 12; for model 5 the distributions are similar. Figure 12 shows that the internal structure of APBs in the $L1_0$ phase is not very sensitive to the type of interaction, similarly to the case for the $L1_2$ phase illustrated by figure 6. However, this structure strongly depends on the alloy composition and appears to again reveal a microstructural 'proximity effect' discussed above in sections 3 and 4.

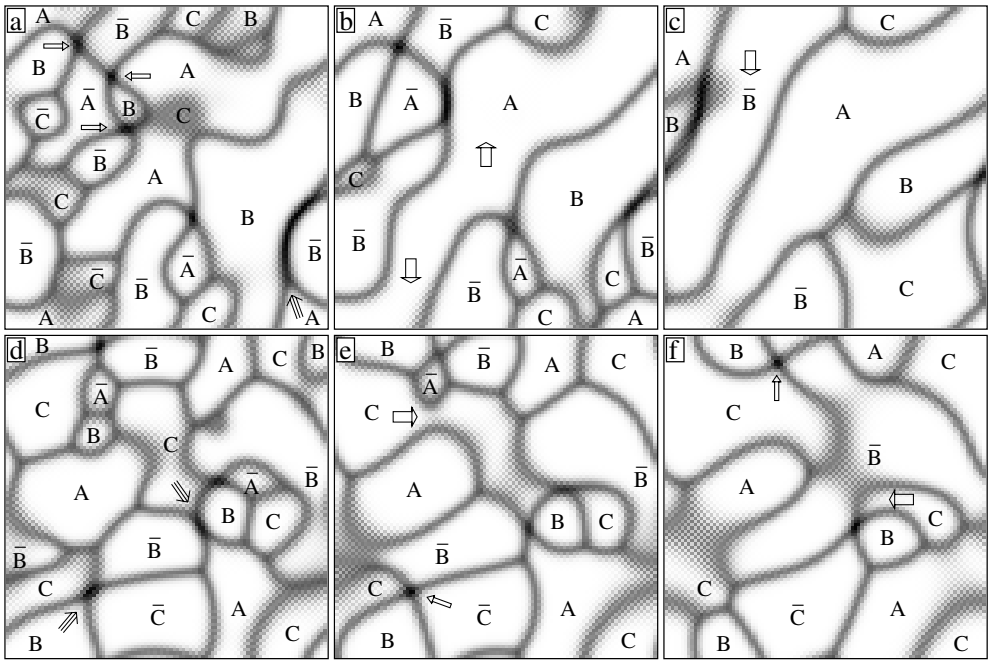

Figure 17. As figure 15, but for 3D simulation with $V_b = 50^3$ and the following values of t': (a) and (d), 5; (b) and (e), 10; (c) and (f), 20. Frames (a), (b), and (c) correspond to the plane $z = 15a$; and frames (d), (e), and (f), to the plane $z = 30a$.

6. Conclusions

Let us summarize the main results of this work. We study the microstructural evolution under the $L1_0$- and $L1_2$-type orderings in alloys. To this end we apply the earlier-described kinetic cluster-field approach to simulate A1 $\rightarrow$ $L1_0$ and A1 $\rightarrow$ $L1_2$ transformations after a quench of an alloy from the disordered A1 phase to the single-phase $L1_0$ or $L1_2$ field of the phase diagram. We employ five alloy models with different types of interaction, from the short-range-interaction model 1 to the extended-range-interaction model 5. We use both 2D and 3D simulations, and all significant features of evolution in both types of simulation were found to be similar. In these simulations we neglect the deformations of the crystal lattice, in particular, the tetragonal distortion of the $L1_0$-ordered antiphase domains (APDs). Thus in the consideration of the A1 $\rightarrow$ $L1_0$ transformation our results correspond to its initial stage (or to the alloy systems for which the tetragonal distortion is small) when the lattice deformations are not yet essential for the microstructural evolution.

In consideration of the A1 $\rightarrow$ $L1_2$ transition we studied the concentration dependence of the evolution. This dependence was found to be particularly pronounced for the intermediate-range-interaction systems, such as our model 4. For the extended-range-interaction systems, such as our model 5, the evolution is less sensitive to the concentration, similarly to the case for the short-range-interaction systems discussed earlier [7]. On the other hand, the internal structure of APBs in the $L1_2$ phase shows significant compositional changes. This structure appears to be mainly determined by the location of the concentration–temperature point c, T in the phase diagram, in particular, by the distance Δ between this c, T point and the nearest two-phase region $L1_2$ + X: the smaller Δ, the closer the APB structure to

that characteristic of the phase X. In particular, at values of c, T close to the two-phase region $L1_2 + A1$ the APBs show a significant local disorder, while near the two-phase region $L1_2 + L1_0$ the APBs show a high degree of local $L1_0$ order. Similarly, the structure of APBs in the $L1_0$ phase near the $L1_0 + L1_2$ two-phase region shows a significant degree of local $L1_2$ order. Such a microstructural 'proximity effect' could be a general feature of the APB structure in ordered alloys.

We also studied a peculiar mechanism of domain growth under the $A1 \rightarrow L1_2$ transformation, the fusion of different in-phase domains, and found it to usually be important for evolution. We observed two types of such fusions: those due to a break of the contact between two adjacent APDs which initially separate the in-phase domains to be fused, and those due to the disappearance of an intermediate domain that initially separates two in-phase domains to be fused, and both these types of fusion were observed with a similar frequency.

Simulations of the $A1 \rightarrow L1_0$ transformation were made at both stoichiometric and off-stoichiometric concentrations, $c = 0.5$ and $c = 0.44$. The main microstructural difference from the $A1 \rightarrow L1_2$ transition is due to the presence under the $L1_0$ ordering of six types of APD and two different types of APB separating APDs with the same or with perpendicular tetragonal axes ('shift-APBs' and 'flip-APBs'), while there are only four types of APD and one type of APB for the $L1_2$ ordering. However, our simulations reveal a number of microstructural similarities between the $A1 \rightarrow L1_0$ and $A1 \rightarrow L1_2$ transitions at the stages of evolution considered, in particular, for short-range-interaction systems such as our models 1, 2, and 3. Transient microstructures in such systems under the $L1_0$ ordering include mainly the (100)-oriented conservative APBs, particularly at stoichiometric concentration $c = 0.5$, and both the distribution of APBs and the evolution kinetics reveal a number of peculiar features analogous to those discussed earlier [7] for the $A1 \rightarrow L1_2$ transition.

The concentration dependence of the evolution under the $A1 \rightarrow L1_0$ transition for the short-range-interaction systems was found to be sharper than that under the $A1 \rightarrow L1_2$ transition: the energetic preference of conservative APBs in the $L1_0$ phase appears to decrease with the deviation from stoichiometry much more rapidly than that in the $L1_2$ phase, and microstructures at off-stoichiometric $c = 0.44$ reveal a much more isotropic distribution of APBs and a higher evolution rate than those at stoichiometric $c = 0.5$.

In all our simulations of the $A1 \rightarrow L1_0$ ordering, particularly for the systems with an intermediate or extended interaction range, we observed the fusion-of-domain processes mentioned above for the $A1 \rightarrow L1_2$ transition. There are two versions of the 'break-of-the-contact' process for the $L1_0$ ordering which correspond to a break of a shift-APB or a flip-APB, and the breaks of shift-APBs were observed much more frequently, particularly at significant deviations from stoichiometry.

Our simulations also reveal the presence of some peculiar microstructural features specific to the $A1 \rightarrow L1_0$ transformation. First, there are the quadruple junctions of four domains (4-junctions) which are long-living transient configurations corresponding to some local minima in the configurational alloy energy. There are two types of such junctions, the 'stable' and the 'metastable' ones described in section 5, and both of them are typical for the microstructures with mainly non-conservative APBs, i.e. for the alloy systems with an interaction range R_{int} that is not small or at significant deviations δc from stoichiometry.

The other characteristic feature of the $L1_0$ ordering in such systems is the presence of numerous processes of 'splitting' of a shift-APB into two flip-APBs which reflects a decrease of stability of shift-APBs relative to flip-APBs under an increase of R_{int} or δc. The stability or metastability of 4-junctions mentioned above is also related to a high excess energy of shift-APBs which makes a decay of such junction with the formation of a shift-APB energetically unfavourable.

Acknowledgments

The authors are much indebted to V Yu Dobretsov, G D Samolyuk and K D Belashchenko for their help in this work, as well as to Georges Martin, for numerous stimulating discussions. The work was supported by the Russian Fund of Basic Research under Grants No 00-02-17692 and 00-15-96709.

References

[1] Chen L-Q, Wang Y Z and Khachaturyan A G 1994 *Statics and Dynamics of Alloy Phase Transformations (NATO Advanced Study Institute, Series B: Physics, vol 319)* ed A Gonis and P E A Turchi (New York: Plenum) p 587
[2] Dobretsov V Yu, Martin G, Soison F and Vaks V G 1995 *Europhys. Lett.* **31** 417
[3] Dobretsov V Yu, Vaks V G and Martin G 1996 *Phys. Rev.* B **54** 3227
[4] Gorentsveig V I, Fratzl P and Lebowitz J L 1997 *Phys. Rev.* B **55** 2912
[5] Frontera C, Vives E, Castan T and Planes A 1997 *Phys. Rev.* B **55** 212
[6] Kikuchi R and Cahn J W 1979 *Acta Metall.* **27** 1337
[7] Belashchenko K D, Dobretsov V Yu, Pankratov I R, Samolyuk G D and Vaks V G 1999 *J. Phys.: Condens. Matter* **11** 10 593
[8] Belashchenko K D, Samolyuk G D and Vaks V G 1999 *J. Phys.: Condens. Matter* **11** 10 567
[9] Zhang B, Lelovic M and Soffa W A 1991 *Scr. Metall.* **25** 1577
[10] Tanaka Y, Udoh K-I, Hisatsune K and Yasuda K 1994 *Phil. Mag.* A **69** 925
[11] Oshima R, Yamashita M, Matsumoto K and Hiraga K 1994 *Solid–Solid Phase Transformations* ed W C Johnson *et al* (Warrendale, PA: The MMM Society) p 407
[12] Yanar C, Wiezorek J M K and Soffa W A 2000 *Phase Transformations and Evolution in Materials* ed P E A Turchi and A Gonis (Warrendale: The MMM Society) p 39
[13] Vaks V G 1996 *Pis. Zh. Eksp. Teor. Fiz.* **63** 447 (Engl. Transl. 1996 *JETP Lett.* **63** 471)
[14] Belashchenko K D and Vaks V G 1998 *J. Phys.: Condens. Matter* **10** 1965
[15] Kikuchi R 1951 *Phys. Rev.* **81** 988
[16] Finel A 1994 *Statics and Dynamics of Alloy Phase Transformations (NATO Advanced Study Institute, Series B: Physics, vol 319)* ed A Gonis and P E A Turchi (New York: Plenum) p 495
[17] Vaks V G and Samolyuk G D 1999 *Zh. Eksp. Teor. Fiz.* **115** 158 (Engl. Transl. 1999 *Sov. Phys.–JETP* **88** 89)
[18] Chassagne F, Bessiere M, Calvayrac Y, Cenedese P and Lefebvre S 1989 *Acta Metall.* **37** 2329
[19] Loiseau A, Ricolleau C, Potez L and Ducastelle F 1994 *Solid–Solid Phase Transformations* ed W C Johnson *et al* (Warrendale, PA: The MMM Society) p 385
[20] Potez L and Loiseau A 1994 *J. Interface Sci.* **2** 91